Stony Brook University

Investigation of the Spectral Properties of Martian Chloride-bearing Deposits as Observed by CRISM and THEMIS

A Thesis Presented

by

Heidi Bundgaard Jensen

to

The Graduate School

in Partial Fulfillment of the

Requirements

for the Degree of

Master of Science

in

Geosciences

Stony Brook University

December 2011

Stony Brook University

The Graduate School

Heidi Bundgaard Jensen

We, the thesis committee for the above candidate for the

Master of Science degree, hereby recommend

acceptance of this thesis.

Timothy D. Glotch– Thesis Advisor
Associate Professor, Department of Geosciences

Deanne Rogers– Second Reader
Assistant Professor, Department of Geosciences

Brian Phillips – Third Reader
Professor, Department of Geosciences

This thesis is accepted by the Graduate School

Lawrence Martin
Dean of the Graduate School

Abstract of the Thesis

Investigation of the Spectral Properties of Martian Chloride-bearing Deposits as Observed by CRISM and THEMIS

by

Heidi Bundgaard Jensen

Master of Science

in

Department of Geosciences

Stony Brook University

2011

The initial identification of proposed chloride-bearing deposits on Mars by the Mars Odyssey Thermal Emission Imaging System (THEMIS) inspired a series of remote sensing studies investigating its geological context and morphology. This thesis focuses on spectral properties observed in remote sensing data for proposed chloride-bearing deposits. In Chapter 2, the issue of connecting the near infrared (NIR) spectral character of these deposits to chloride minerals is approached. In Compact Reconnaissance Imaging Spectrometer for Mars (CRISM) near infrared (1.1 – 2.5 μm) reflectance data for these deposits, a red slope (increase in reflectance with increasing wavelength) is observed in spectral ratios where the chloride-bearing region spectrum is divided by a spectrally neutral pyroxene-bearing region spectrum. This spectral character is inconsistent with the NIR spectral character of chloride minerals observed in the laboratory. Whereas the lack of features present in this wavelength region supports the hypothesis that these deposits are chloride-bearing, this spectral character is observed for unoxidized sulfide minerals and homopolar compounds (such as diamond) as well. NIR spectra

of 1) simple mixtures of halite with labradorite and flood basalt and 2) halite crusts formed on labradorite and flood basalt were divided by spectra of pure labradorite or flood basalt, to see if the featureless red slope observed in CRISM ratio spectra could be emulated. These mixtures were formed with a variety of grain sizes in order to see if particle size has any effect on the ratio spectral shape. In order to rule out the possibility of unoxidized sulfides, acid washed pyrite was also mixed with labradorite and flood basalt of varying grain sizes, to see if the ratio spectra of these mixtures to pure labradorite/ flood basalt could also imitate the remote sensing spectral character. The results of this study allow unoxidized sulfide to be ruled out spectrally, and give some constraints on the composition and grain size of the chloride mixtures/ crusts that make up the Martian chloride-bearing deposits.

Chlorides were originally discovered based on their unusual thermal infrared (TIR) spectral properties, characterized by featureless blue sloping (decrease in emissivity with increasing wavelength) spectra with a higher emissivity between 1267.62 and 850.846 cm^{-1} than the surrounding basaltic materials. Variations in the strength of the chloride unit spectral slope variations have not been previously investigated. Of particular interest is to identify potential factors resulting in chloride unit spectral slope variation that are not due to the mineralogy of the surface. The two factors investigated in this study are the characteristics of the TES training region used to manually correct for the atmosphere in the THEMIS data and the THEMIS image collection conditions. The result of this work indicates a weak correlation between chloride unit spectral slope and the minimum surface emissivity of the TES training region. Image acquisition conditions do not result in large differences in spectral character, but the quality of the atmospheric correction likely does influence the strength of the chloride unit spectral slope. Until chloride spectral variation that is not the product of surface mineralogy can be fully controlled,

the spectral properties cannot be used to estimate characteristics such as the composition or chloride abundance.

Dedication Page

This thesis is dedicated to my parents, for always been there for me and guiding me towards the person that I have grown to become.

Table of Contents

List of Figures

List of Tables

Acknowledgments

A few people deserve credit for their contributions to the work presented in this thesis. The work presented in Chapter 2 is in press in *JGR Planets* with my advisor Tim Glotch as coauthor. Tim provided valuable guidance and constructive criticism in the process of both conducting the laboratory experiments and creation of the manuscript. Bill Woerner provided X-ray diffractions patterns and compositional information for all rock and mineral powders used in this study. Alex Smirnov provided assistance in the process of using the ball mill and acid washing the pyrite powders.

The work presented in Chapter 3 would not have come together without the direction and knowledge that I have received in the past three years from Tim. I remember meeting with Tim the summer before I began my graduate studies here at Stony Brook University and wondering how I would learn about Mars, learn how to work on linux-based machine and figure out how to navigate “the squiggly lines” of remote sensing. He has always been there for the worried emails and random questions throughout the years and I hope that he realizes how much I appreciate what he has done for me.

1. Introduction

The identification of proposed chloride mineral deposits on the Martian surface using Mars Odyssey Thermal Emission Imaging System (THEMIS) false color mid-infrared images has resulted in some controversy due to the observed spectral character of these deposits [*Osterloo et al*., 2008; *Osterloo et al*., 2010]. Generally, mineral identification from infrared data is made based on the presence of diagnostic absorptions at specific wavelengths. However, the mid-infrared spectra of anhydrous chloride minerals collected in the laboratory display featureless spectra with nonunit maximum emissivity (values less than one). Figure 1-1 displays the THEMIS mid-infrared spectral character for these deposits in comparison with the basaltic regional terrain, where the chloride deposits display blue sloping (decrease in emissivity with increasing wavelength) spectra with a local emissivity minimum at band 5 (9.35 μm, 1075.09 cm^{-1}). The observed slopes in the THEMIS data for these units has been proposed to be the result of the assumption that unit emissivity occurs in the data during the conversion from radiance to emissivity, whereas the local minimum emissivity at band 5 has been proposed to be the result of mixture with regional basaltic materials [*Osterloo et* al., 2008; *Bandfield*, 2009; *Osterloo et al*., 2010]. Though previous studies have identified the spectral character of these deposits in general and revealed their geological context, spectral variation between deposits has not been examined.

Near infrared hyperspectral image cubes chloride units collected by the Compact Reconnaissance Imaging Spectrometer for Mars (CRISM) aboard the Mars Reconnaissance Orbiter (MRO) reveal red sloping (increasing reflectance with increasing wavelength) featureless ratio spectra in the 1.1 - 2.5 μm (9090.9 – 4000 cm^{-1}) wavelength range which is inconsistent with laboratory spectra collected for anhydrous chloride minerals [*Murchie et al*., 2009; *Wray et*

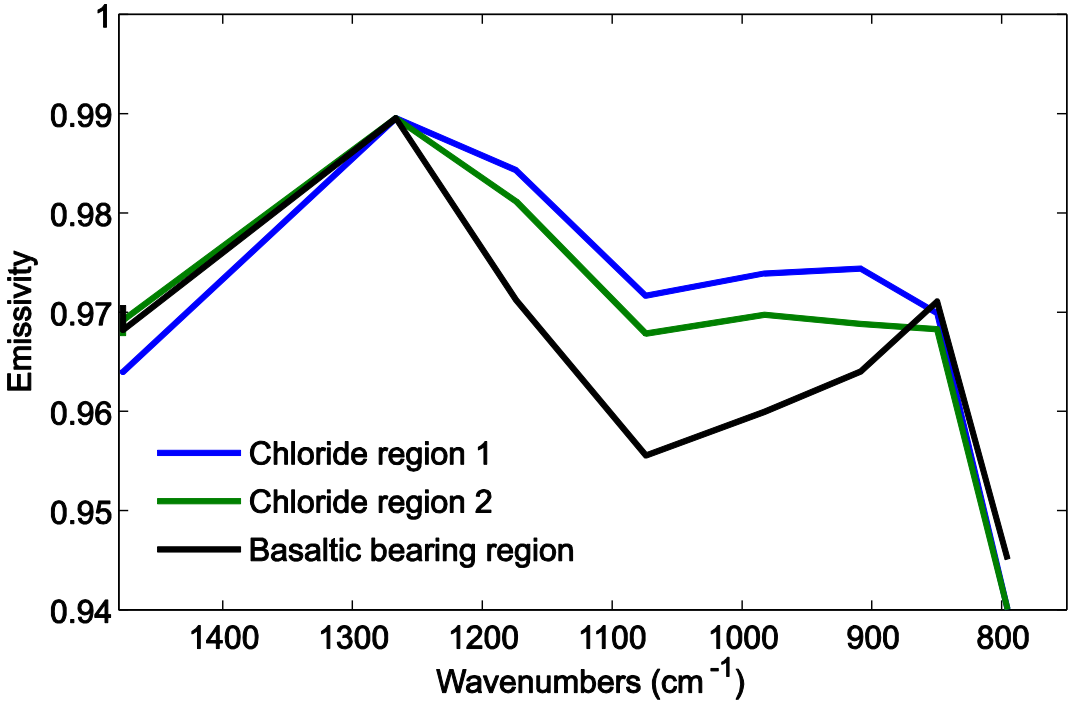

Figure 1-1. THEMIS spectra of 2 chloride-bearing regions and a proximal basaltic region from THEMIS image I17455004. The spectra have been corrected to account for atmospheric attenuation and atmospheric emission.

al., 2009; *Glotch et al*., 2010]. Whereas chlorides have been suggested to be the mineral responsible for the observed featureless spectral character, unoxidized sulfides and homopolar compounds (single element, e.g. diamond) can also result in featureless spectra in this wavelength region. Though unoxidized sulfides and homopolar compounds are unlikely to occur and persist on the Martian surface, they have not previously been ruled out spectrally.

This thesis is divided into two main science chapters with a final chapter that reviews the main conclusions of this work and suggests areas for future work. The study conducted in Chapter 2 suggests that the observed slope in CRISM data could be the result of an admixture of chloride with a spectrally neutral material and rules out the possibility of sulfide as a component in these deposits [*Glotch et al*., 2010; *Jensen and Glotch,* 2011]. In Chapter 2, spectra of simple combinations of halite and acid washed pyrite with labradorite and flood basalt of various grain sizes were collected. These mixtures were ratioed to pure labradorite/ flood basalt spectra of the same grain size to imitate the way in which CRISM data is divided by spectra of the surrounding terrain and compared to the proposed chloride spectral character observed in CRISM ratio spectral data. This chapter has been submitted to the *Journal of Geophysical Research – Planets,* and is currently in press. The results of this study show that pyrite mixtures could not produce the observed CRISM spectral character of chloride deposits due to the rapid oxidation of pyrite resulting in a feature centered at ~1.7 μm. Simple anhydrous halite mixtures with labradorite and halite crusts on labradorite were shown to be capable of producing red sloping featureless spectra in almost all of the grain sizes and halite proportions investigated. The success of the flood basalt mixtures with halite and halite crusts on flood basalt were more restricted, which has implications for chloride deposits on the Martian surface which is largely basaltic in composition.

In Chapter 3, the spectral variability of chloride deposits in THEMIS data due to two potential factors is investigated. The first is the selection of TES training regions used in manual atmospheric correction of the data. The second is THEMIS data collection conditions. A total of 109 THEMIS images were investigated to observe overall spectral variability of chloride deposits, with 57 images atmospherically corrected with more than one TES training region and in 10 cases overlapping THEMIS images collected at different times of the Martian year were investigated. The chloride unit spectral slope between bands 3 (7.889 μm, 1267.62 cm^{-1}) and 8 (11.753 μm, 850.846 cm^{-1}) was used as a proxy for spectral variability. The results of this study show that only the minimum emissivity of the TES training region shows any correlation with changes in the chloride unit spectral slope, and this correlation is very weak. The distance from the area(s) of interest and surface temperature of the TES training region, surface temperature ranges of the THEMIS images induced by seasonal variations of THEMIS image collection and location of the chloride unit within the THEMIS image area do not predictably change the chloride unit spectral slope.

2. Investigation of the Near Infrared Spectral Character of Putative Martian Chloride Deposits

2.1. Introduction

The presence of putative chloride salt-rich deposits in the southern highlands of Mars was originally observed in Mars Odyssey Thermal Emission Imaging System (THEMIS) daytime mid-infrared images. These features display a blue slope (decrease in emissivity with increasing wavelength) in the 7.93-12.57 μm region compared to the surrounding terrain. The deposits can be easily identified by their distinctive aqua color in THEMIS band 9, 6, 4 (12.57, 10.21, and 8.56 μm, respectively) decorrelation stretched (DCS) images [*Gillespie et al*., 1986; *Osterloo et al.*, 2008, 2010; *Glotch et al.*, 2010]. Data covering these deposits from the Compact Reconnaissance Imaging Spectrometer for Mars (CRISM) instrument on board the Mars Reconnaissance Orbiter (MRO) also display a unique spectral character in the near infrared (NIR) spectral range in overlapping full resolution targeted (FRT) and half resolution long targeted (HRL) images [*Murchie et al*., 2009; *Wray et al*., 2009; *Glotch et al*., 2010]. These putative chloride-rich units exhibit featureless spectra in CRISM L spectrometer NIR data, with a red slope (increase in reflectance with increasing wavelength) in the 1.1-2.6 μm range and an inverted hydration feature in the 3 μm region when ratioed to a spectrally neutral region within the CRISM image. Throughout the southern highlands of Mars, many occurrences of smectite clays are found adjacent to these units of interest, suggesting that these sites were in contact with liquid water over long time periods [*Murchie et al*., 2009; *Wray et al.*, 2009]. In Terra Sirenum, where the largest co-occurrence of phyllosilicates and putative chlorides are observed on Mars, CRISM data also reveal the presence of vermiculite and/or a smectite/chlorite interlayer clay in close association with the putative chloride-rich material, suggesting that diagenesis occurred

after initial phyllosilicate deposition [*Milliken and Bish*, 2010; *Glotch et al*., 2010]. The occurrence of these mineral assemblages suggests a diverse aqueous history in which parts of the ancient Noachian crust were altered by liquid water [e.g., *Wray et al*., 2009].

Some unoxidized sulfides and anhydrous chlorides exhibit featureless spectra throughout the spectral range of both THEMIS and CRISM [*Hunt et al*., 1971; *Hunt et al*., 1972]. Whereas unaltered sulfides are unlikely to exist in close proximity to phyllosilicate deposits, they have yet to be ruled out spectrally. Sulfide minerals would most likely be oxidized and converted to sulfates upon persistent exposure to aqueous weathering processes at the surface of Mars [*Burns and Fisher*, 1993; *Zolotov and Shock*, 2005]. Both unoxidized sulfides and anhydrous chloride salts lack red slopes in the 1.1-2.6 μm region in laboratory spectra (Figure 2-1), suggesting that this characteristic in CRISM ratio spectra could be the result of an admixture of anhydrous chloride salts or unoxidized sulfides with the surrounding materials [*Clark et al.*, 2007]. In this work, we acquired NIR (1.1-2.5 μm) spectra of mixtures of halite and pyrite with labradorite and flood basalt standards. The goals of this study are to determine if chloride salts or sulfides mixed with these silicate phases can reproduce the featureless, red-sloped spectra observed in CRISM data.

2.2. Background

2.2.1. Halite

2.2.1.1. Halite on Earth

Terrestrial chloride deposits form by (1) precipitation from an evaporating or freezing surface composed of surface water, groundwater, or hydrothermal brines, (2) crystallization directly onto sediment grains (efflorescence), or (3) condensation of volcanic gases [*Bernard and Le Guern*, 1986; *Symonds et al.*, 1987; *Goodall et al.*, 2000]. Playas are a well-studied and

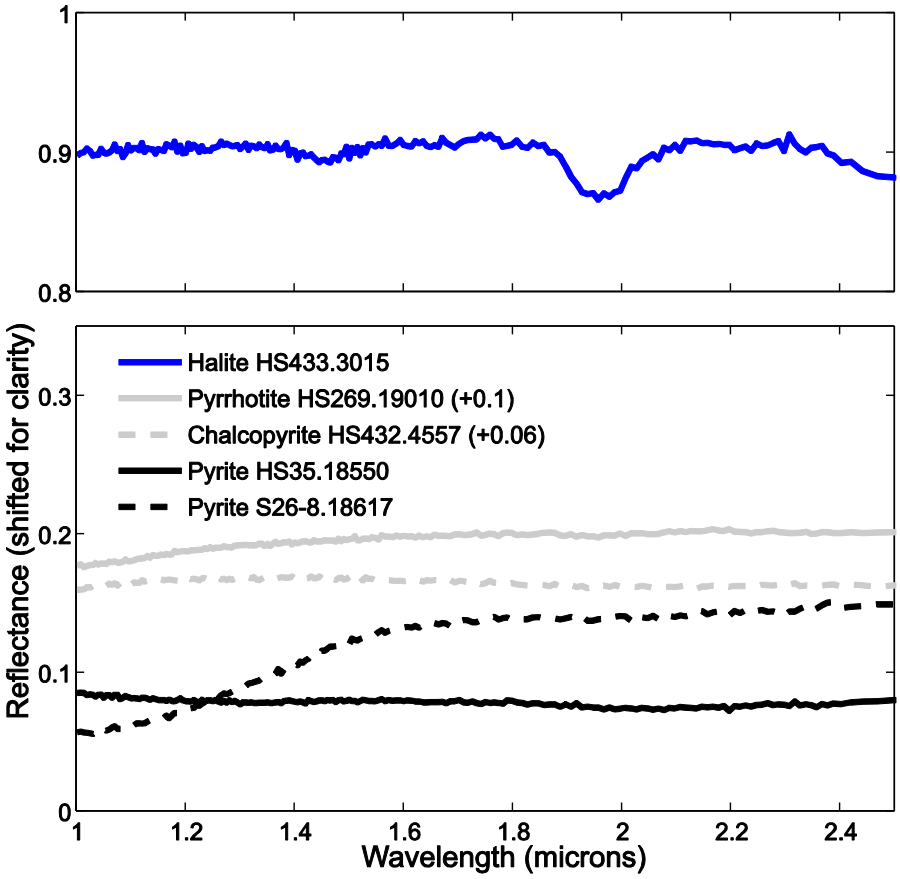

Figure 2- 1. NIR reflectance spectra of halite, pyrrhotite, chalcopyrite and 2 pyrites from the U.S. Geological Survey (USGS) spectral library [Clark et al., 2007]. Numbers in parentheses indicate the amount that some spectra were shifted for clarity. Absorptions in the halite spectrum centered at 1.4 and 1.9 μm are hydration features.

common terrestrial environment in which massive evaporitic deposits, including chloride salts, can be observed due to alternating wet and dry periods, high evaporation rates and their hydrologic isolation in closed basins [*Hardie et al*., 1978]. The brine compositions of terrestrial saline lakes (CaMgNa(K)Cl, Na(Ca)SO_4Cl, MgNa(Ca)SO_4Cl, $NaCO_3$Cl, and $NaCO_3SO_4$Cl) and subsequent precipitates are dependent on the chemical weathering reactions produced by the inflowing waters. The ubiquitous presence of sodium in these brines results from the weathering of feldspars, the dissolution of halite and some atmospheric sources [*Hem*, 1992; *Eugster and Hardie*, 1978]. The first minerals to precipitate from an evaporating brine are generally carbonate and gypsum followed only much later in brine evolution by halite and other chlorides due to their extremely high solubilities [*Eugster and Hardie*, 1978]. These evaporitic environments can result in spatially extensive, thick chloride deposits such as those found in Death Valley, California.

Whereas terrestrial saline lakes are a large source, volcanic sublimates from fumaroles are also a source of chloride salt deposition. In condensation studies conducted using fumarole gases of Mount St. Helens in Washington state and the Merapi Volcano in Indonesia, gases emitted were condensed in silica tubes resulting in the formation of both halite and sylvite in the range of 550-450 ºC [*Bernard and Le Guern*, 1986; *Symonds et al*., 1987]. At higher temperatures, magnetite, cristobalite, molybdenite, and ferberite crystalized and at lower temperatures sulfides, including greenockite (CdS) and galena (PbS) condensed out of the gaseous phase [*Bernard and Le Guern*, 1986]. Whereas fumaroles result in the deposition of chloride minerals, deposits from these sources are not laterally or vertically extensive.

2.2.1.2. Halite in SNCs

Only two of the 97 approved SNC (Shergottites, Nakhlites, and Chassignites) meteorites, Nakhla and Shergotty, possess secondary mineralogy that includes the presence of halite based

on petrographic observations [*Gooding et al*., 1990*; Gooding et al*., 1991; *Bridges et al.*, 2001]. The SNC meteorites are thought to have originated from Mars based on their long range of ages, trapped gas compositions, fractionated bulk and trace elemental compositions and oxidation of the observed mineral assemblages [*Bridges and Grady*, 2000 and sources therein]. In Nakhla, halite is present as (1) an interstitial component with segregated clusters of one or more crystals of up to 400 μm in size, (2) a coating with anhydrite covering plagioclase and silica grains, and (3) the filling of veins in association with siderite and anhydrite adjacent to interstitial areas [*Bridges and Grady*, 1999; *Bridges et al.*, 2001]. *Bridges and Grady* [2000] suggested a progressive evaporation model in which the secondary mineralogy corresponds with the extent of evaporation where Lafayette, Governador Valadares and Nakhla have >20 %, 15-20 %, and <10 % water remaining. All three Nakhlites contain goethite and apatite, with Lafayette representing the initial precipitates from the brine with Ca-rich siderite and smectite/illite followed by Governador Valadares which has siderite, smectite/illite, gypsum and anhydrite followed by the final stage of precipitation in Nakhla with Mg-, Mn-rich siderite, smectite/illite, halite and $MgSO_4$. In Shergotty, minor isolated occurrences of Mg-chloride are present with halite as the dominant chloride occurring as vein filling material, a covering of silicate surfaces in rounded patches, and variably weathered individual or clumped halite grains [*Wentworth et al.*, 2000]. *Bridges et al.* [2001] suggest that the source of this secondary mineralogy in both Nakhla and Shergotty is the evaporation of low temperature (25-150 ^{0}C) brines. Their study also suggests that the presence of high sulfur and chloride concentrations in Martian soils may have resulted from the redistribution of these deposits by aeolian processes.

2.2.1.3. In situ observation of halogens on Mars

Through data collected by the X-ray fluorescence spectrometers (XRF) aboard the two Viking landers, the alpha proton X-ray spectrometer (APXS) aboard Pathfinder's Sojourner and

the alpha particle X-ray spectrometers (APXS) aboard the Mars Exploration Rovers (MER), we have been able to collect geochemical data, including Cl and Br concentrations, at the Martian surface. From the 17 samples analyzed with high precision from Chryse Planitia (Viking Lander 1) and Utopia Planitia (Viking Lander 2), Viking XRF data suggest that Martian fines have higher concentrations of Cl than terrestrial soils, with a range of 0.3-0.9 wt. % [*Clark et al.*, 1982]. Data collected from the soils and rocks of Ares Vallis by the APXS instrument on the Sojourner rover revealed a mean value of 0.55 wt. % Cl in Pathfinder soils and a calculated value of 0.32 wt. % chloride for soil-free rocks [*Brückner et al.*, 2003]. In the first 1368 sols of the Spirit rover's journey, the APXS instrument observed 0.1-1.9 wt. % Cl in the soils and rocks of the Gusev plains and Columbia Hills [*Gellert et al.*, 2006, *Ming et al.*, 2008]. In the first 90 sols of the Opportunity rover's travels, its APXS revealed Cl concentrations in the rocks ranging 0.06-0.44 wt. % on surfaces on which the rock abrasion tool (RAT) was used and 0.54-0.68 wt. % on unabraded surfaces. Opportunity's APXS also revealed Cl concentrations in the Meridiani Planum soils ranged from 0.33-0.54 wt. % [*Rieder et al.*, 2004].

Aqueous chemical analyses of the northern plains of Vastitas Borealis by the Wet Chemistry Laboratory (WCL) on the Phoenix Mars Lander indicate that Cl is present in perchlorate minerals in this region of Mars [*Hecht et al.*, 2009]. This detection of perchlorate in the soils at the Phoenix lander site brings to question the source of elemental Cl detections by the other rover missions. Whereas the Viking, Sojourner, MER Opportunity and Spirit rovers all detected Cl in the soils and rocks that they analyzed, some proportion of that Cl could be held in perchlorates and not chloride minerals.

2.2.2. Sulfides

2.2.2.1. Sulfides on Earth

On Earth, sulfides are present as components of hydrothermal veins (e.g., black smokers), pegmatites, contact-metamorphic deposits, and stratiform sedimentary environments [*Deer et al*., 1992]. Sulfide mineral deposits in the form of stratabound lenses or sheets with thicknesses of up to a few meters can be found at the base of magnesian ultramafic lava flows (komatiites) and have been proposed to be present on Mars as well [*Guilbert and Park*, 1986; *Burns and Fisher*, 1990]. Upon exposure of sulfide minerals to the surface by mining practices or uplift, interaction with surficial oxygenated water results in oxidation to form a large array of sulfate minerals and oxyhydroxides as well as acidification of surface waters [*Jambor et al*., 2000]. Gossans, which are capping units composed mainly of iron oxides and quartz, are formed when ore deposits containing sulfide minerals interact with cyclic surface water, leaching sulfides and primary ore materials, resulting in supergene enrichment at depth [*Guilbert and Park*, 1986].

2.2.2.2. Sulfides in SNCs

Sulfides are present in SNC meteorites as minor components. An array of Fe-sulfides have been observed, including pyrrhotite ($Fe_{(1-x)}S$ (x = 0 to 0.2)), troilite (Fe_7S_8, also given as $Fe_{(1-x)}S$), pyrite (FeS_2), chalcopyrite ($CuFeS_2$), pentlandite $(Fe,Ni)_9S_8$ and marcasite (FeS_2) as minor accessory phases in SNC meteorites in petrographic studies [*McSween*, 1985]. A stepped combustion experiment performed on Shergotty, ALHA 77005, Chassigny and Nakhla produced concentrations of sulfur as sulfide ranging from 75 ppm in Nakhla to 1665 ppm in Shergotty with bulk sulfur ranging from 220 to 1930 ppm [*Burgess et al.*, 1989]. A study of 6 shergottites, including 2 olivine-phyric and 4 basaltic Shergottites, via electron microprobe revealed ranges of sulfide from 0.16 to 0.53 area % [*Lorand et al.*, 2005].

2.2.2.3. In situ observations of sulfur on Mars

X-ray spectrometer data from NASA's landers and rovers on the Martian surface have provided information about the overall sulfur concentration of soils and rocks. The 17 samples

with high precision analysis collected from both Viking lander sites revealed that (1) Martian fines have higher concentrations of sulfur than soils on Earth, (2) sulfur is positively correlated with chlorine, and (3) sulfur accounts for 5.9-9.5 % of the elemental composition of the fines as SO_3 [*Clark et al.*, 1982]. The Mars Pathfinder Sojourner rover APXS revealed the mean S content of soils at 2.7 wt. %, cemented soil at 2.5 wt.% and the calculated soil-free rock at 0.3 wt. % [*Brückner et al.*, 2003]. The Spirit rover revealed S concentrations ranging from 1.09-35.1 wt. % sulfur as SO_3 from the beginning of its mission to sol 1368 [*Gellert et al.*, 2006; *Ming et al.*, 2008]. In comparison, data from the first 90 sols of the Opportunity rover data collection revealed 4.52-7.29 wt. % sulfur as SO_3 [*Rieder et al.*, 2004]. It should be noted that all elemental values of sulfur on the surface collected by rover instruments have been reported as SO_3.

A few in situ observations of unoxidized sulfide were observed by the Mössbauer instruments aboard the Opportunity and Spirit rovers. Based on Mössbauer data collected by the Opportunity rover, the stony-iron meteorites Barberton, Santa Catarina, Santorini and Kasos are inferred to contain troilite [*Schröder et al.*, 2008, 2010; *Fleischer et al.*, 2010]. These four stony-iron meteorites have been paired based on their chemical and mineralogical similarities, despite being observed over a distance of ~10 km in Opportunity's roving path [*Schröder et al.*, 2008, 2010; *Fleischer et al.*, 2010]. The Spirit rover's Mössbauer data suggest the possible presence of pyrite or marcasite in a loose rock located atop the Home Plate outcrop named Fuzzy Smith [*Squyres et al.*, 2007; *Morris et al.*, 2008,]. The detection is based on the presence of the Fe?D1 doublet in the Mössbauer data which is from low-spin Fe^{2+}, indicating FeS_2, or tetrahedral (tet)-Fe^{3+}, possibly a phyllosilicate [*Squyres et al.*, 2007; *Morris et al.*, 2008]. Fuzzy Smith has an unusual chemical composition that has not been observed by either rover; high Zn, the highest Si, K and Ge measured at Gusev crater, and very low Ca and Fe [*Squyres et al.*, 2007]. The

chemical and mineralogical data for Home Plate suggest a volcanic origin for Fuzzy Smith [*Squyres et al.*, 2007].

The Wet Chemistry Laboratory (WCL) on NASA's Phoenix Mars Lander reported soluble sulfate equivalent to ~1.3 (±0.5) wt. % as SO_4 in the soil around the lander, probably as $CaSO_4$ and/or $MgSO_4$ [*Kounaves et al.*, 2010]. Another result from the Phoenix lander's WCL is a sulfur (as SO_4^{2+}) to total chloride (Cl^- and ClO_4^-) ratio of ~2:1 [*Kounaves et al.*, 2010]. This is quite different from the relatively constant S/Cl ratio of ~4:1 observed by previous XRF. *Kounaves et al.* [2010] explain that this discrepancy may be due to soils in this region being chemically different than those observed by other rover/landers or some of the sulfur collected by the WCL was not/sparingly soluble.

2.2.2.4. Martian sulfide geochemistry

The presence of widespread sulfates on the surface of Mars observed both in situ by rovers/ landers and by remote sensing instruments leads to questions about their source(s). *Burns and Fisher* [1993] hypothesized that percolating water containing oxidants (dissolved oxygen and Fe^{3+}) from photolysis of water vapor could initiate a set of reactions to form clays, sulfates and iron oxyhydroxides. Another hypothesis, based on laboratory simulations, is that sulfates could be produced by regional heating releasing sulfide-rich hydrothermal waters from the subsurface resulting in near-surface oxidation of pyrite-rich deposits [*Zolotov and Shock*, 2005]. A series of weathering experiments using metallic iron (α-Fe), magnetite, and pyrrhotite under simulated Martian conditions resulted in the production of elemental sulfur, sulfates, goethite and siderite in the case of metallic iron and iron sulfide [*Chevrier et al.*, 2004]. The extensive observation of sulfates and other oxidation products, as well as the lack of crustal recycling by plate tectonics on Mars suggests that sulfide deposits on the Martian surface are not likely to persist over geologic time scales.

2.3. Data, Samples and Methods

CRISM Full Resolution Targeted (FRT) and Half Resolution Long Targeted (HRL) data were analyzed for regions that displayed putative chloride salt deposits in THEMIS daytime infrared DCS images, with confirmed spectral character from extracted atmospherically corrected THEMIS emissivity spectra from the images. CRISM color composite images were made using CRISM summary products [*Pelkey et al.*, 2007; *Murchie et al.*, 2009]. In some regions, putative chloride salts are in close association with phyllosilicates [*Glotch et al.*, 2010]. To display phyllosilicates in association with the chloride deposits, red, green and blue were assigned to the inverse of the IR spectral slope parameter (chloride), D2300 (2.3 μm drop-off, phyllosilicate), and LCPINDEX (low calcium pyroxene), respectively (Figure 2-2b). The volcano-scan correction technique was used to remove atmospheric absorptions present in the CRISM I/F data [*McGuire et al.*, 2009]. Spectra were extracted from atmospherically corrected CRISM hyperspectral image cubes by averaging pixels over areas bearing chloride (red) and phyllosilicate (green) signatures. In order to remove remnant atmospheric effects and instrumental calibration artifacts, spectra were then ratioed to regions in the image that were considered to be spectrally neutral (Figure 2-2c). In this case, pyroxene-bearing areas were used since dusty regions (which are generally spectrally neutral) within the images were absent.

2.3.1. Sample Description

Natural samples of flood basalt, labradorite, and pyrite were obtained from Ward's Natural Science, and halite was acquired from Acros Organics (reagent grade 99 %+ synthetic sodium chloride). Labradorite and flood basalt were chosen for use in this study due to the lack of strong absorptions within the spectral range. Labradorite mixtures and crusts represent a simple single mineral example and flood basalt mixtures and crusts represent a more realistic

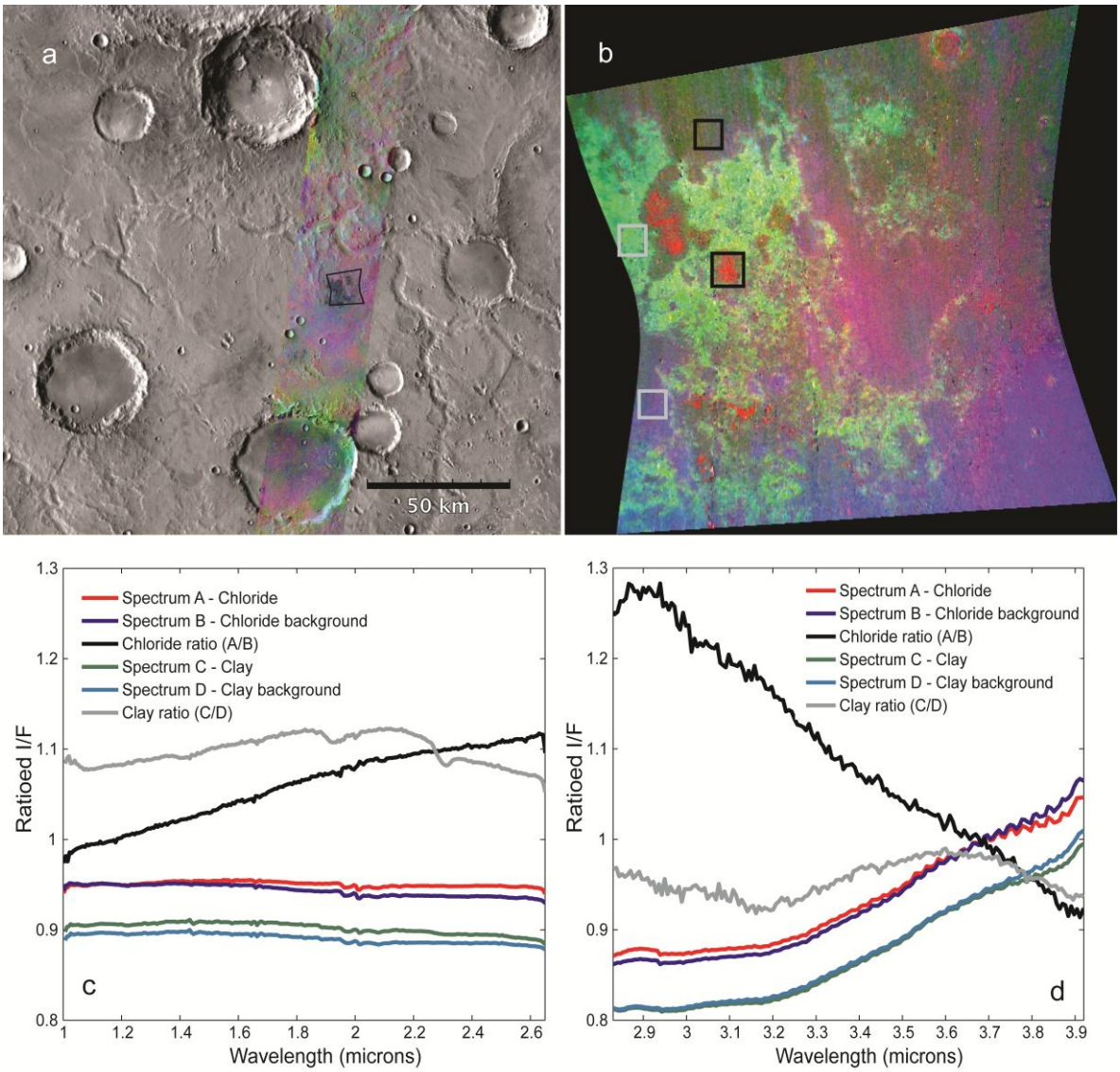

Figure 2- 2. CRISM images depicting phyllosilicate-bearing and chloride-bearing regions, along with their characteristic NIR spectra. a) THEMIS daytime IR DCS (9, 6, 4) image I01835005 showing the location of the CRISM image FRT00009ACE overlain onto the THEMIS daytime IR map. Image is centered at 353.5 ºE, -5.5 ºN. b) CRISM color composite image of FRT00009ACE where red, green and blue correspond to the reverse of the ISLOPE1, D2300 (2.3 µm drop off), and LCPINDEX parameters, respectively [*Pelkey et al*., 2007]. Chlorides appear red and phyllosilicates appear green. The image is ~ 10 km across. Black boxes indicate the location of pixels averaged for the chloride-bearing region and background spectra and gray boxes indicate the location of pixels averaged for the phyllosilicate-bearing region and background spectra in c) and d). c) Characteristic CRISM ratio spectra of chloride-bearing units with a proximal phyllosilicate-bearing unit for comparison along with the raw numerator and denominator averaged spectra in the 1.1 – 2.5 µm wavelength range. d) Characteristic CRISM ratioed and raw spectra in the 2.8 – 3.92 µm wavelength range. The chloride ratio spectrum indicates that the chloride units are more desiccated than the nearby pyroxene-bearing pixels averaged and used as the denominator spectrum.

rock composition for comparison with the Martian surface. Halite as the chloride mineral used in this study due to its availability and relative stability in comparison with $MgCl_2$ and other anhydrous chlorides. Acid-washed pyrite was chosen due to its availability, and is assumed to be a proxy for other unoxidized Fe-sulfides. NIR spectra of many natural Fe sulfides have an absorption at ~1 μm due to the Fe^{2+} crystal field band (Figure 2-1). This absorption can be due to either the Fe^{2+} in the sulfide, an Fe oxide or hydroxide or another impurity phase.

In order to achieve desired size fractions, flood basalt and labradorite were crushed in a tool steel mortar and pestle, halite was ground in an agate mortar and pestle and pyrite was ground using an automated agate ball mill. All ground samples were then dry sieved to several grain size fractions (Table 1). Particles of ≤10 μm grain size were separated using Stokes' settling method [*Day*, 1965; *Gee and Bauder*, 1986; *Salemi et al.*, 2010]. Settling was conducted at 22 ^{0}C in a 600 mL beaker using HPLC (high-performance liquid chromatography) grade distilled water (ethanol was used for the settling of halite) and the supernatant containing the ≤10 μm size fraction was removed and placed into a beaker using a 100 mL glass pipette. After the sample had completely settled out of solution, excess water/ethanol was removed by pipette and the sample was dried in an 80 ^{0}C oven (ethanol was removed through evaporation).

Table 2- 1. Prepared size fractions for materials used in this study.

Mineral/Rock	≤10 μm	63-90 μm	125-180 μm	180-250 μm	250–355 μm
Labradorite	X	X	X	X	
Flood basalt	X	X	X		X
Halite	X	X	X	X	X
Acid-washed pyrite	X	X			

Pyrite powders were acid washed with 1.0M deoxygenated HCl solution in a nitrogen environment for ≥30 minutes and subsequently rinsed with deoxygenated deionized water in a vacuum filtration system in a nitrogen glove box free of oxygen. Acid washing was necessary to

ensure that oxidation products (primarily Fe sulfates and Fe oxide/hydroxides) were not present [e.g., *Karthe et al.*, 1993; *Elsetinow et al.*, 2003]. While in the nitrogen glove box, approximate masses of pyrite were weighed out and then transported in a sealed vial to the Vibrational Spectroscopy Laboratory (VSL) for precise weight measurements prior to mixing. Accurate weight measurements could not be measured in the nitrogen glove box on the available balance. Great care was taken to ensure that the sample mixtures were not oxidized before spectral analysis.

Diffuse reflectance spectra were collected from 1-2.5 μm for all grain sizes of the labradorite, flood basalt, halite and acid-washed pyrite used in this study (Table 1, Figure 2-3). The spectra for labradorite slope upwards towards longer wavelengths (red slope), with absorptions located at ~1.4, 2.2, 2.35 and ~2.45 μm due to a muscovite impurity and absorptions at ~1.9 μm due to hydration of the samples (Figure 2-3a). The presence of muscovite is supported by the powder diffraction pattern of this sample (discussed below). Flood basalt powders display red sloping diffuse reflectance spectra, with absorptions located at ~1 and ~2.3 μm due to the presence of clinopyroxene and absorptions at ~1.9 μm due to hydration of the samples (Figure 2-3b). Halite samples reveal relatively featureless red sloping diffuse reflectance spectra with the only absorptions located at ~1.9 μm due to hydration (Figure 2-3c). Diffuse reflectance spectra of acid-washed pyrite also display red sloping spectra with broad absorptions located at ~1 and ~2 μm (Figure 2-3d). These absorptions in the acid-washed pyrite are due to either the incomplete removal of oxidation products in the acid washing process, oxidation of the pyrite in the time that it was exposed to ambient air or the natural spectral character of pyrite itself. It should be noted that the presence of slopes in these diffuse reflectance spectra are likely

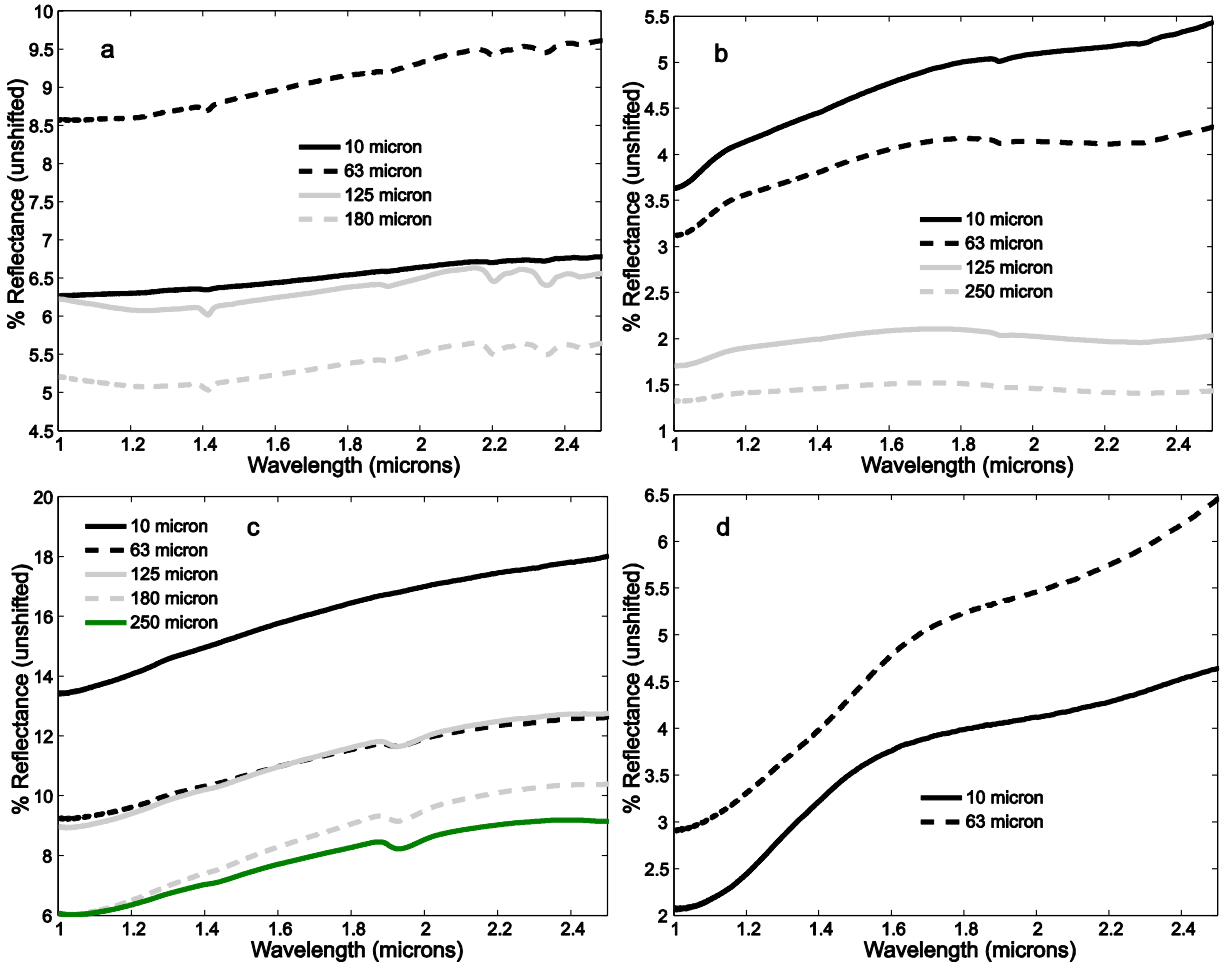

Figure 2- 3. Diffuse reflectance spectra of a) labradorite, b) flood basalt, c) halite and, d) acid-washed pyrite for all grain sizes used in this study.

due to the use of a first surface gold mirror instead of MgO or spectralon as a reflectance standard. Since spectral ratios are used in this study for comparison to CRISM ratio spectra; the choice of reflectance standard does not affect the results.

Powder diffraction patterns were collected to assess sample purity on a Rigaku Ultima IV X-ray diffractometer using Cu k$\alpha_{1,2}$ radiation, a DteX LPSD detector, 2.5 degree soller slits and a 0.01 degree step size. Data were collected at a rate of 0.5 degree 2θ per minute. The powder diffraction patterns for the halite (10-120 degrees 2θ) and pyrite (20-110 degrees 2θ) samples reveal no impurities. The labradorite diffraction pattern (5-90 degrees 2θ) matches that of a sample from Labrador, Canada described as An52 and contains impurities that make up only a few wt. % of the sample. These impurity phases include a K-rich feldspar (likely orthoclase), kaolinite and muscovite. The flood basalt powder diffraction pattern (10-90 degrees 2θ) reveals a composition of major plagioclase and minor clinopyroxene. Based on lattice parameters, the plagioclase phase in the flood basalt is about An50 or less. The clinopyroxene phase in the flood basalt is of space group C2/c indicating that it is in the range of diopside, augite and hedenbergite. The clinopyroxene peaks in the flood basalt diffraction pattern are broadened, possibly indicating chemical inhomogeneity.

2.3.2. Halite and Pyrite Mixtures

Silicate samples with the grain fractions listed in Table 1 were mixed with halite in proportions of 1, 10, 50 and 75 wt. % halite. Additionally, Flood basalt mixtures with halite were also made with 25 wt. % halite. Samples were gently mixed to obtain sample homogeneity and maintain grain size. These mixtures were then placed in a vacuum oven at 150 ^{0}C for ≥5 days to remove surface-adsorbed water. Upon removal from the oven, samples were stored in a desiccator cabinet prior to spectral analysis.

We also prepared 25 and 50 wt. % mixtures using the acid-washed pyrite. Since only the ≤10 and 63-90 μm acid-washed pyrite size fractions were available, mixtures were only made using the ≤10, 63-90 and 125-180 μm grain sizes of the mixture rock and minerals. The comparatively larger density and smaller grain size of the pyrite resulted in heterogeneous mixing for larger size fractions.

In addition to the particulate mixtures described above, we created a series of salt-crusted samples. Flood basalt and labradorite were added to sample vessels until they were two-thirds full (about 0.3 g) and then topped off with a saturated halite solution made with HPLC grade distilled water. These vessels were then stored in a desiccator for >3 days to evaporate the water and form a crust on the sample surface. If necessary, additional halite saturated solution was added followed by desiccation to form a relatively smooth surface for NIR analysis.

2.3.3. Visible and Near Infrared (VNIR) Reflectance Measurements

The dried sample mixtures were placed into a sample cup and diffuse near infrared (0.8-2.5 μm) reflectance spectra were collected on the Stony Brook University Vibrational Spectroscopy Laboratory's Nicolet 6700 FTIR spectrometer equipped with a diffuse reflectance attachment, a CaF_2 beamsplitter and an uncooled InGaAs detector. For each sample, 1024 scans were recorded in the NIR spectral range using a white light source and a spectral resolution of 4 cm^{-1}. Spectra of the mixtures where then ratioed to spectra of pure labradorite or flood basalt of the same grain size to facilitate direct comparison to CRISM ratio spectra. A first surface gold mirror was used as a standard reference.

2.4. Laboratory Results

Table 2-2 summarizes the results of the laboratory work, indicating which samples produced featureless red slopes in ratio spectra.

Table 2- 2. Halite mixtures, pyrite mixtures and halite crusts that exhibit a featureless red slope in NIR ratio spectra with additional absorptions attributable to either hydration or impurities. Mixtures with halite were made with halite of the same size fraction as the labradorite or flood basalt. For acid-washed pyrite mixtures ≤10 micron acid-washed pyrite was mixed with ≤10 micron labradorite/ flood basalt whereas 63-90 µm acid-washed pyrite was mixed with both 63-90 and 125-180 µm labradorite/ flood basalt.

Mineral/ Rock, grain size	1% halite	5% halite	10% halite	25% halite	50% halite	75% halite	halite crust	25% pyrite	50% pyrite
Flood basalt, ≤10 µm									
Flood basalt, 63-90µm	X	X	X	X					
Flood basalt, 125-180µm	X	X	X	X			X		
Flood basalt, 250-355µm							X		
Labradorite, ≤10 µm			X	n.a.	X	X	X		
Labradorite, 63-90µm	X	X	X	n.a.	X	X			
Labradorite, 125-180µm	X	X	X	n.a.	X	X	X		
Labradorite, 180-250µm	X	X	X	n.a.	X	X	X		

2.4.1. Halite mixtures

2.4.1.1. Mixtures with labradorite

Halite mixtures with labradorite result in red slopes in spectral ratios of the mixtures to pure labradorite for almost all samples, with a few exceptions (Figure 2-4). The ≤10 µm mixtures with halite proportions of 1 and 5 wt. % result in a blue featureless slope. The 180 µm grain size 5 wt. % halite mixture results in a flat spectrum, with no overall slope. The presence of a muscovite impurity in the labradorite used in these experiments can be observed throughout the halite mixtures with labradorite. This impurity can be observed in the ratioed spectra as absorptions and ratio reflectance maxima at 1.4 µm, corresponding to overtones of the O-H stretching modes, as well as at 2.2, 2.35 and ~2.45 µm, corresponding to the metal-OH combination stretching plus bending vibrational bands. In many of the ratio spectra, and particularly noticeable in the 50 wt. % mixtures, there is a broad hump between 1.4 and 1.9 µm that may be induced by the absorptions attributable to the muscovite impurity. A general trend is

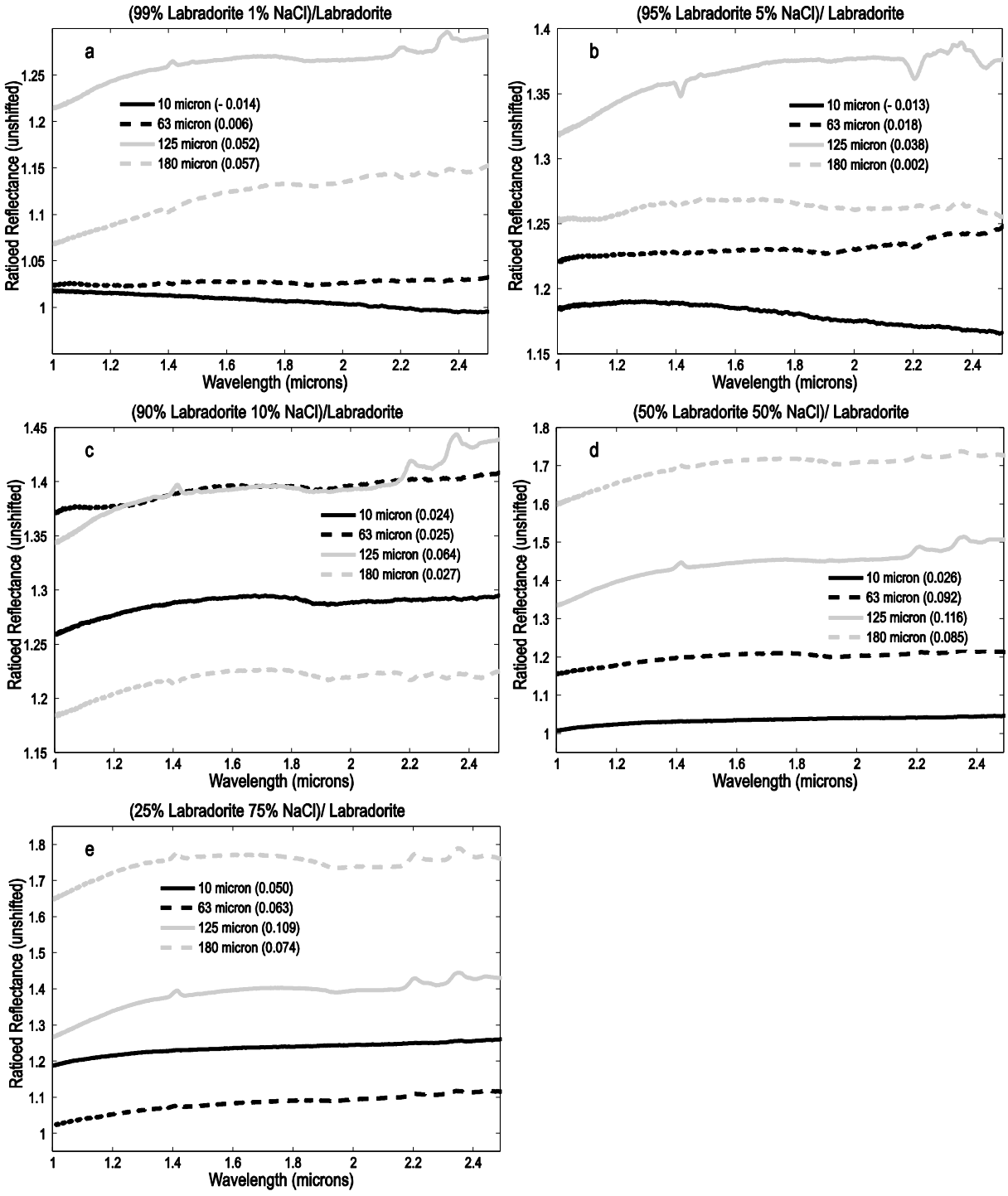

Figure 2- 4. Ratio spectra for halite mixtures with labradorite with a) 1 wt. % halite, b) 5 wt. % halite, c) 10 wt. % halite, d) 50 wt. % halite, and e) 75 wt. % halite. Absorptions and negative absorptions located at 1.4, 2.2, 2.35 and ~2.45 µm are due to a muscovite impurity. The numbers in parentheses after the grain size labels in the legend indicate the spectral slope, rounded to the nearest thousandths.

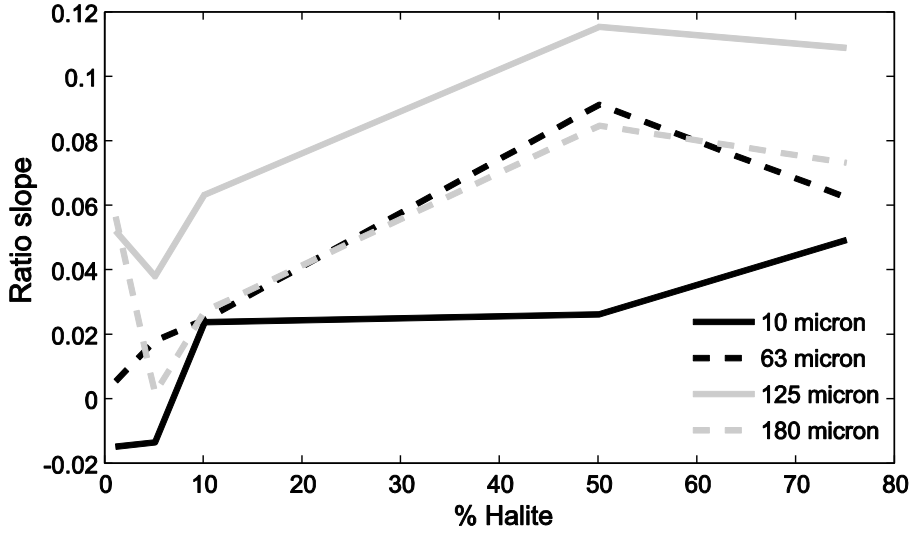

Figure 2- 5. Plot of ratio spectral slope versus halite proportion for each grain size of labradorite.

observed that with increasing halite proportion, the slope towards longer wavelengths of the ratio spectra is generally increased for mixtures of all grain sizes (Figure 2-5). In summary, from 1 wt. % to 75 wt. % halite mixtures, a red slope is maintained in the ratio spectra with other absorptions attributed to the muscovite impurity in the labradorite, with a few noted exceptions.

2.4.1.2. Mixtures with flood basalt

Spectral ratios of halite mixtures with flood basalt to pure flood basalt spectra are shown in Figure 2-6. Halite mixtures of grain sizes of ≥63 μm, with 1-25 wt. % halite result in an increase in reflectance with increasing wavelength observed in ratioed reflectance. At 75 wt. % halite and above, a red slope is not clearly observed and a broad absorption is present in the ratio spectra between 1.2 and 2 μm due to the inversion of the flood basalt's clinopyroxene absorptions at ~1 and 2.3 μm (Figure 2-6f). For the 50 wt. % halite mixture of 63-90 μm grain size, the red slope is negligible and the 75 wt. % halite mixture has a blue slope. The 250-355 μm ratio spectra for all halite proportions except 1 wt. % clearly display an inversion of the clinopyroxene absorptions of the flood basalt. The ≤10 μm grain size mixtures for all proportions of halite display a blue slope. Hydration of the halite mixture with respect to the pure flood basalt can be observed in the ratio spectra as an absorption at 1.9 μm, corresponding to combination tones of the fundamental bending and stretching vibrations of H_2O. A ratio reflectance maximum at this wavelength results from the flood basalt sample being more hydrated with respect to the halite mixture. Figure 2-7 displays the relationship between ratio spectral slope and halite proportion for each grain size mixture with flood basalt.

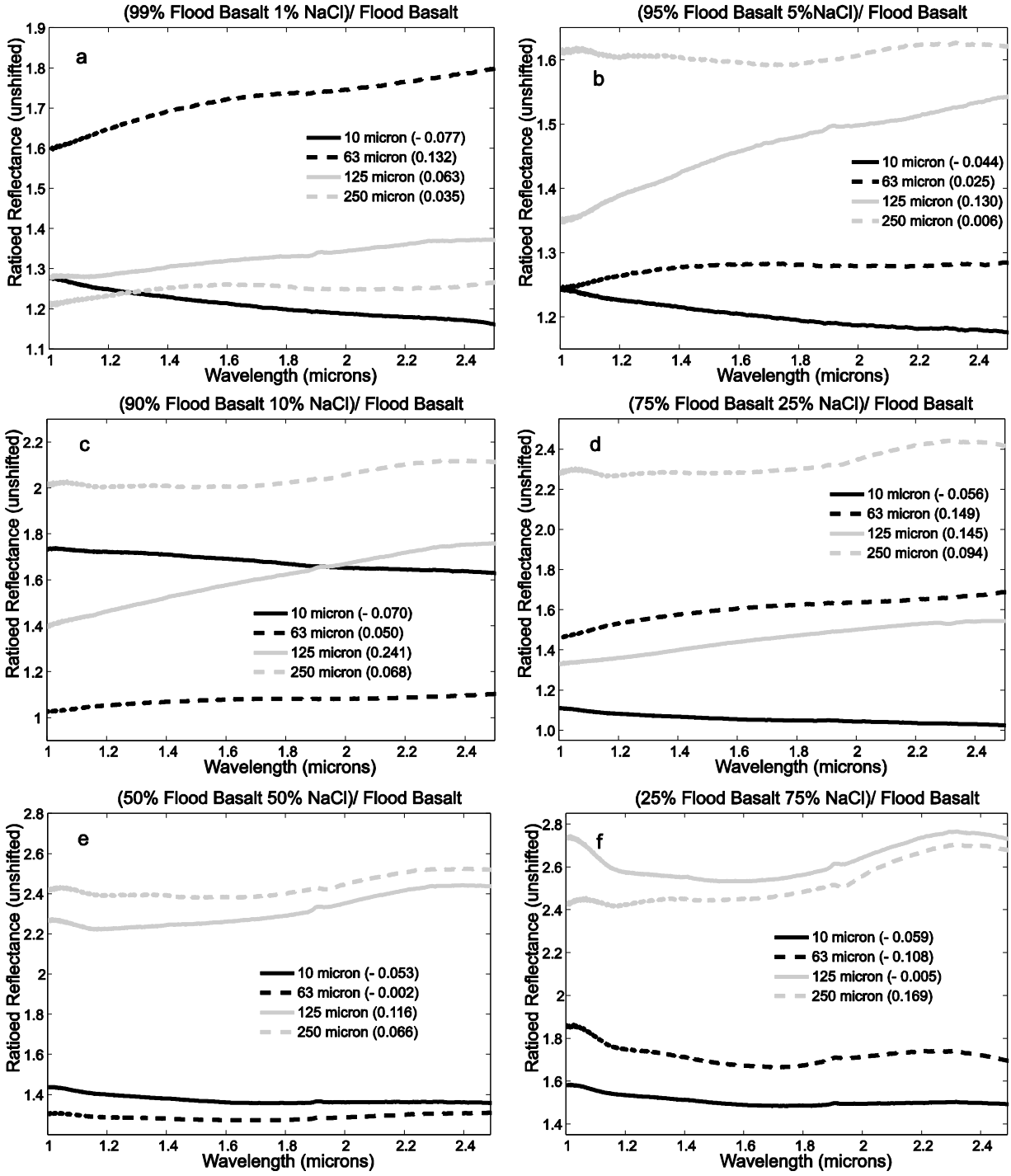

Figure 2- 6. Ratio spectra for halite mixtures with flood basalt with a) 1 wt. % halite, b) 5 wt. % halite, c) 10 wt. % halite, d) 25 wt. % halite, e) 50 wt. % halite, and f) 75 wt. %. The numbers in parentheses after the grain size labels in the legend indicate the spectral slope, rounded to the nearest thousandths.

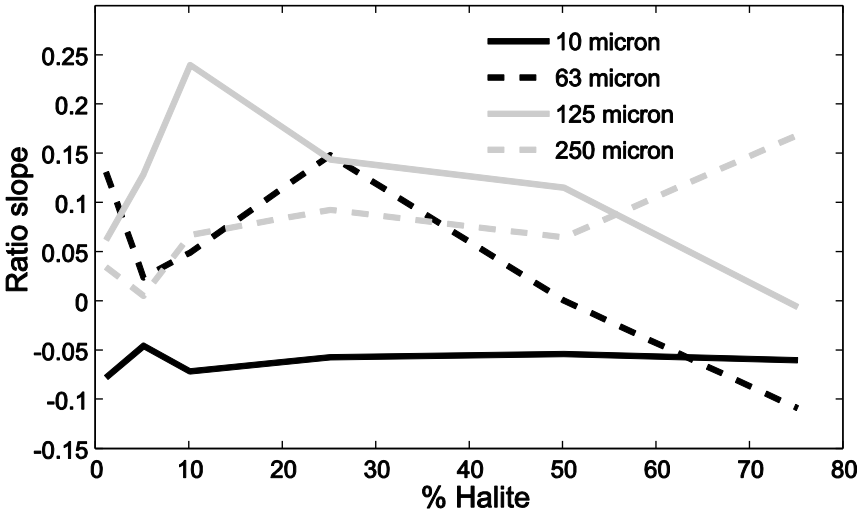

Figure 2- 7. Plot of ratio spectral slope versus halite proportion for each grain size of flood basalt.

2.4.2. Halite crusts

2.4.2.1. Labradorite salt crusts

In the spectra of the 125-180 and 180-250 μm size fractions, absorptions result from the muscovite impurity in the labradorite sample, but the overall character of the spectral ratio is a red slope (Figure 2-8). A larger overall ratio reflectance value can be observed in the 125-180 μm halite crust sample due to the salt crust having a higher overall reflectance than the labradorite sample used as the denominator. The ≤10 μm grain size labradorite with halite crust sample also results in a slight red slope. The 63-90 μm grain size labradorite with halite crust samples result in a slightly blue sloped spectrum when ratioed to a pure labradorite of the same grain size. An absorption located at 1.9 μm is due to the presence of water not fully removed in the desiccation process of the saturated halite solution used to produce the salt crusts. As was observed in many of the halite/labradorite mixtures, a hump between 1.4 and 1.9 μm, particularly in the ≤10 and 125-180 μm labradorite with halite crust samples, can be seen that is likely caused by absorptions associated with the muscovite impurity in the labradorite.

2.4.2.2. Flood basalt salt crusts

The two larger size fractions of flood basalt, 125-180 and 250-355 μm, resulted in salt crust spectra that produce red slopes when ratioed to pure flood basalt of the same grain size (Figure 2-9). The two smaller size fractions, ≤10 and 63-90 μm, resulted in ratio spectra that sloped downward towards longer wavelengths. The increased ratioed reflectance of the 250-355 μm sample is due to the larger overall reflectance of the halite crust spectrum with respect to the pure flood basalt spectrum used to produce the ratio. The absorption at 1.4 μm in the ≤10 and 250-355 μm grain size samples and at 1.9 μm in all flood basalt crust samples results from remnant water due to incomplete desiccation of the crust samples.

2.4.3. Pyrite mixtures

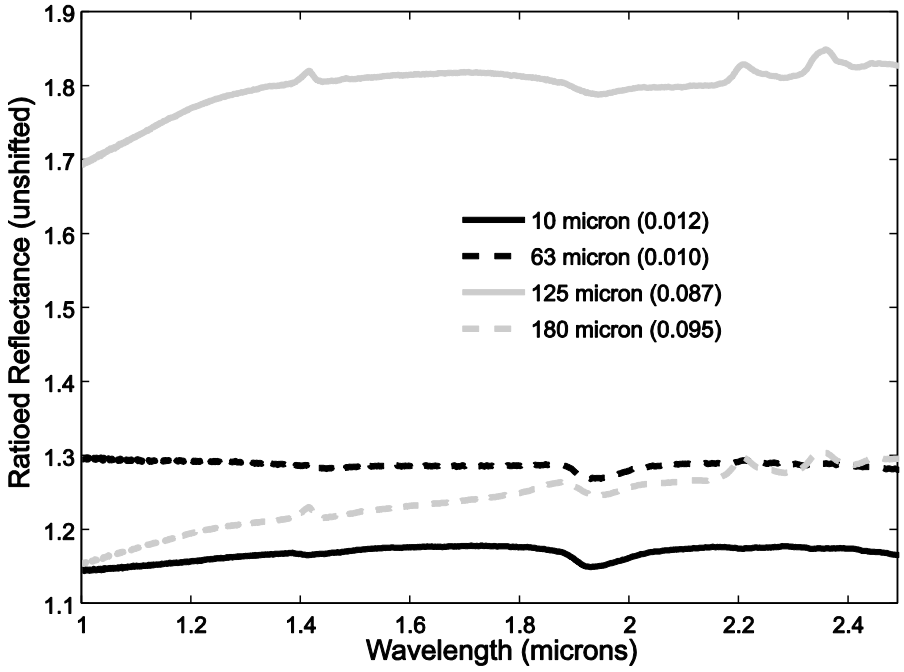

Figure 2- 8. Ratio spectra for halite crusts on labradorite of given size fractions. The numbers in parentheses after the grain size labels in the legend indicate the spectral slope, rounded to the nearest thousandths.

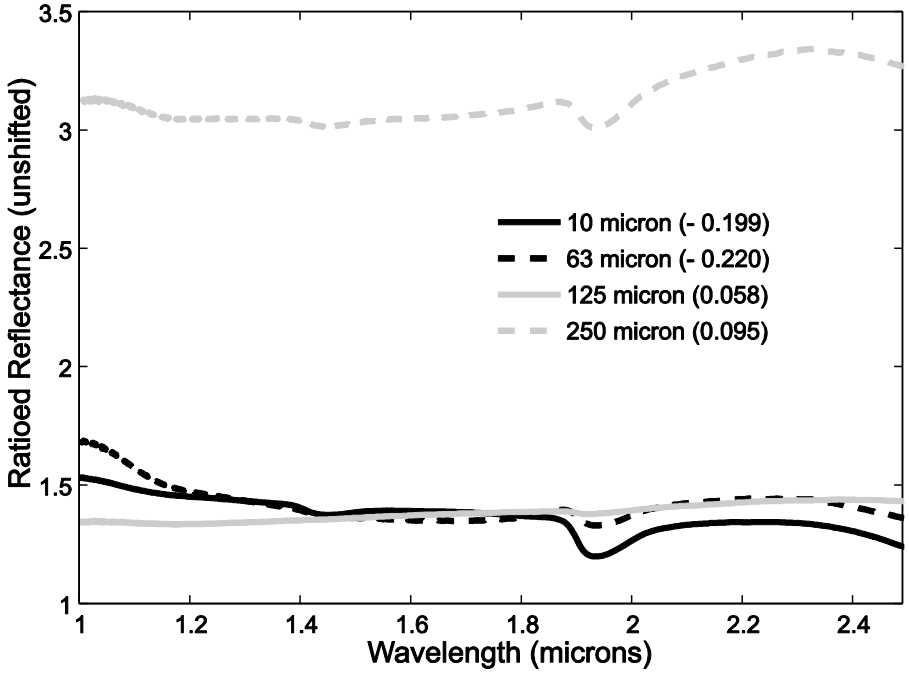

Figure 2- 9. Ratio spectra for halite crusts on flood basalt of given size fractions. The numbers in parentheses after the grain size labels in the legend indicate the spectral slope, rounded to the nearest thousandths.

2.4.3.1. Mixtures with labradorite

The ratioed reflectance spectra of the 25 and 50 wt. % pyrite mixtures with labradorite can be seen in Figure 2-10a and b, respectively. The ratio spectra of both the 25 and 50 wt. % pyrite mixtures with labradorite to the labradorite standard include a red slope with a broad hump centered at ~1.7 μm for all grain sizes. The 50 wt. % pyrite, 125-180 μm grain size ratio spectrum lacks a slope, but still has the broad 1.7 μm feature. A simple relationship of increasing pyrite proportion resulting in increased slope towards longer wavelengths is observed. Reflectance maxima at 1.4, 2.2, 2.35 and ~2.45 μm again correspond to the presence of muscovite in labradorite. The absorptions at ~1 and 2.2 μm, producing the hump in the spectral ratios at ~1.7 μm, results from either the Fe^{2+} crystal field absorptions due to pyrite itself or the presence of pyrite oxidation products in the form of either Fe oxides or oxyhydroxides. The presence of oxidation products results from their incomplete removal in the acid washing process and/or oxidation from exposure to ambient air in the time period required for sample mixing and preparation for data collection [*Karthe et al.*, 1993; *Swayze et al.*, 2000]. If the pyrite mixtures are allowed to sit in ambient air for longer time periods, the observed broad spectral maximum grows in size. This is especially noticeable in the ≤10 μm size fractions resulting from the extended time period necessary to gently mix and achieve homogeneity of the pyrite and labradorite using a mortar and pestle.

2.4.3.2. Mixtures with flood basalt

In ratioed reflectance spectra, mixtures of 25 and 50 wt. % pyrite resulted in a red slope for all three grain sizes used in this study (Figure 2-11). Excluding the 63-90 μm mixtures, a trend of steepening red slope with increasing pyrite fraction is observed. A noticeable broad hump centered at around 1.6 μm, especially in the ≤10 μm size fraction, likely results from the

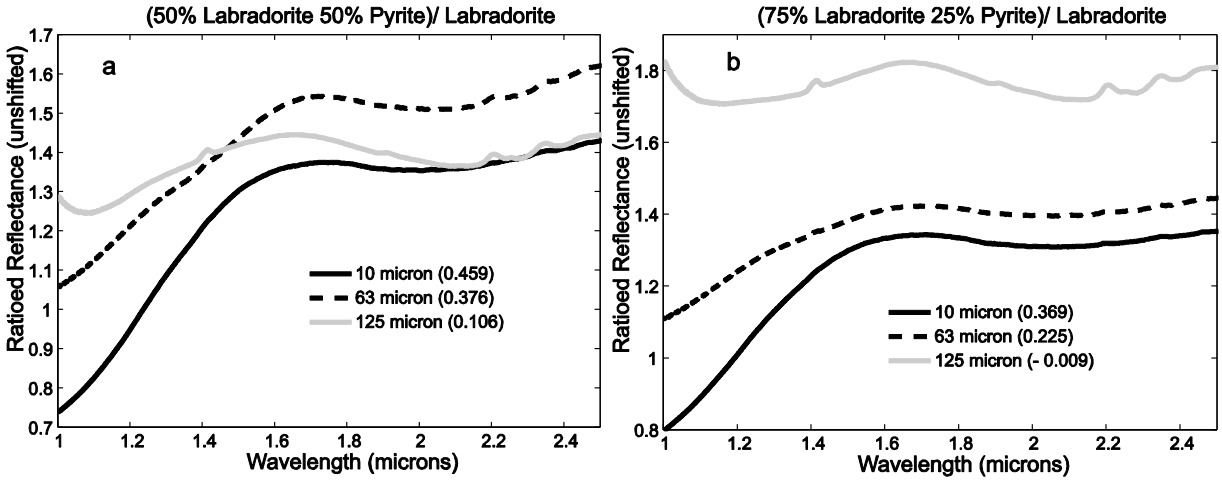

Figure 2- 10. Spectral ratios for mixtures of labradorite with a) 50 wt. % pyrite and b) 25 wt. % pyrite. The numbers in parentheses after the grain size labels in the legend indicate the spectral slope, rounded to the nearest thousandths.

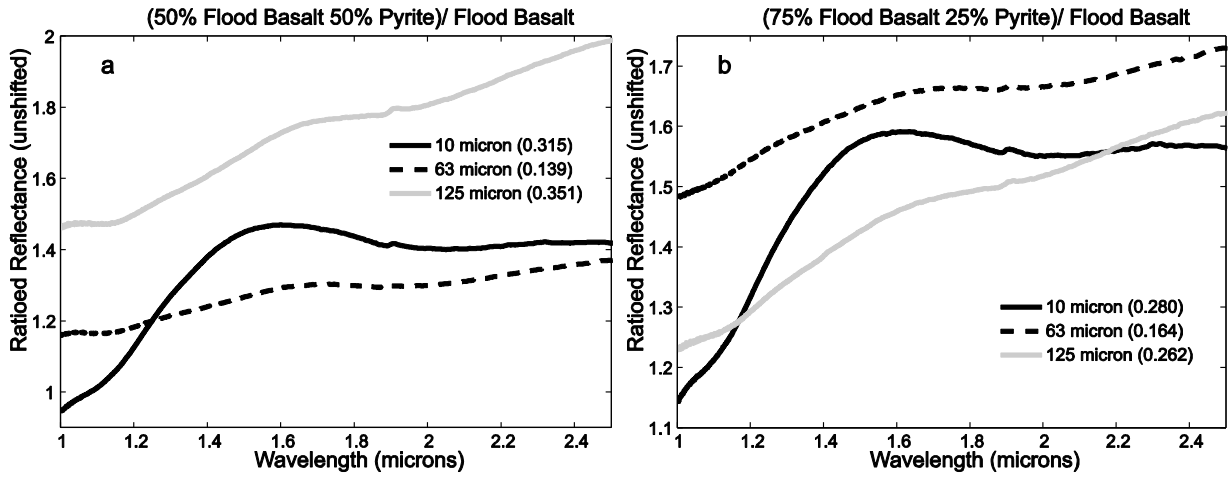

Figure 2- 11. Spectral ratios for mixtures of flood basalt with a) 50 wt. % pyrite and b) 25 wt. % pyrite. The numbers in parentheses after the grain size labels in the legend indicate the spectral slope, rounded to the nearest thousandths.

presence of oxidation products in the pyrite, specifically Fe oxides and hydroxides [*Karthe et al*., 1993, *Swayze et al*., 2000]. A reflectance maximum at 1.9 μm is produced in all ratio spectra, apart from the 50 wt. % pyrite mixture of 63-90 μm particle size, due to hydration of the flood basalt used as the denominator of the spectral ratio with respect to the pyrite mixtures.

2.5. Discussion

Some halite mixtures with labradorite or flood basalt were effective in emulating the featureless red slope previously observed in CRISM data for putative chloride deposits [*Wray et al*., 2009; *Murchie et al*., 2009; *Glotch et al*., 2010]. After accounting for the muscovite impurity present in the labradorite used in this study, all halite proportions mixed with labradorite successfully imitate the NIR remote sensing spectral character, excluding the 1 wt. % and 5 wt. % halite mixtures of ≤10 μm grain size. A hump in many of the labradorite ratio spectra between 1.4 and 1.9 μm, believed to be associated with the presence of muscovite, is observed mainly in the 180 μm mixtures but dominates in 10 wt. % halite spectra of all grain sizes. Fewer flood basalt mixtures are successful in emulating the CRISM ratio spectra. Mixtures composed of 1-25 wt. % halite reveal a featureless red slope for particle sizes of 63-90 and 125-180 μm, other than a hydration feature at 1.9 μm present in many of the ratio spectra. Halite crusts on labradorite emulated a featureless red slope for all but the 63-90 μm grain size fraction, whereas halite crusts on flood basalt were only successful for 125-180 and 250-355 μm grain sizes.

Average thermal inertia values derived for these proposed chloride-bearing units from THEMIS data are >350 $Jm^{-2}K^{-1}s^{-1/2}$, indicating grain sizes greater than ~900 μm or indurated materials [*Presley and* Christensen, 1997; *Mellon et al.*, 2000; *Putzig et al.*, 2005; *Osterloo et al*., 2010]. For labradorite mixtures composed of 1-5 wt. % halite, the ≤10 μm grain size is incapable of producing a red slope whereas larger size fractions are successful. However, for larger halite

proportions, even the ≤10 μm particle size was capable of emulating the featureless red slope found for these deposits in CRISM data. The largest grain size used in the halite/flood basalt mixtures was unable to emulate the CRISM spectral character. Halite crusts on both labradorite and flood basalt produced red slopes only for the for larger grain sizes, consistent with the suggestion from thermal inertia measurements [*Osterloo et al.*, 2010], that the Martian deposits may be indurated.

Halite crusts would be more likely to be formed initially on the Martian surface via groundwater upwelling or pooling of brines on the surface. Late Noachian to early Hesperian crater count-based age estimates for Martian chloride deposits would indicate that these deposits have been exposed to the atmosphere and aeolian processes for ~3.5 Gy or more [*Osterloo et al.*, 2010]. Formation of intimate mixtures, like those in this study, could be produced by extensive aeolian mixing of chloride in the form of surficial crusts with surrounding basaltic materials.

Pyrite mixtures were not capable of imitating the spectral shape observed in the CRISM data for proposed chloride units on the Martian surface. A large hump centered between 1.6 and 1.7 μm, due to rapid oxidation forming Fe – oxides and hydroxides during the sample preparation and data collection time (generally <15 minutes), dominates all pyrite mixture data for both flood basalt and labradorite. Based on the extensive presence of sulfates as well as Fe oxides and hydroxides across the Martian surface observed by both NIR remote sensing instruments and lander/rover data, pyrite would not persist without extensive oxidation. The age of the deposits calculated from crater counting indicates that these units range from late Hesperian to early Noachian (2.6 – 4.1 Gy) [*Tanaka*, 1986; *Tanaka and Hartmann*, 2008; *Osterloo et al.*, 2010]. We conclude that the presence chloride salts is indeed the most likely explanation for these spectrally anomalous units in the Martian southern highlands.

The data we acquired for this study do not allow us to place tight constraints on the abundance of chloride in Martian deposits. The flood basalt results are important since the composition of the Martian crust in the regions where these deposits are observed is mainly Surface Type 1 or Group 2 from TES data [*Bandfield et al*., 2000; *Rogers and Christensen*, 2007]. Surface Type 1 is compositionally similar to terrestrial basalt/ low-Si basaltic andesite containing ~65 vol. % plagioclase and ~30 vol. % clinopyroxene with 45-57 wt. % SiO_2 [*Bandfield et al*., 2000]. Group 2 is defined by the Syrtis TES spectral shape with a derived modal mineralogy of 31 % plagioclase, 29 % high-Ca clinopyroxene, 12 % high-Si phases, 7 % olivine, 4 % orthopyroxene and 17% other (carbonate, sulfate, amphibole, quartz, and alkali-feldspar) [*Rogers and Christensen*, 2007]. Whereas the success of labradorite mixtures was not influenced by halite proportion and only the 1 and 5 wt. % halite mixtures of ≤10 μm grain size were unable to produce the desired spectral character, flood basalt mixtures were more conditionally successful in this study. Flood basalt mixtures of ≤25 wt. % halite and grain sizes between 63 and 180 μm were most effective in producing featureless red slopes in ratio spectra. This is the tightest constraint of possible composition and grain size of these deposits that can be concluded from this NIR study. Slopes produced in ratio spectra from this laboratory study are not quantitatively compared with CRISM ratio spectra because the laboratory ratios were formed using raw diffuse reflectance spectra and the CRISM ratio spectra are based on I/F data. Current studies being conducted in the mid-IR wavelength range of similar mixtures may be able to better constrain chloride abundance and effective grain size for these units.

2.6. Conclusions

In an effort to reproduce the NIR spectral character of putative chloride deposits observed on Mars by the CRISM instrument, simple mixtures of multiple particle sizes were made of

halite/pyrite with flood basalt and labradorite as substrates. Along with these simple mixtures, halite salt crusts were formed on the surfaces of flood basalt and labradorite of varying grain sizes.

The halite mixtures and salt crusts proved to be successful in producing the desired spectral character in many cases. Other than the ≤10 μm size fraction mixtures with halite of the two smallest proportions, all of the labradorite mixtures produced red sloping spectra, with spectral features easily attributable to water associated with the halite or a muscovite impurity within the labradorite. The success of halite mixtures with flood basalt was more limited; proportions of >25% halite resulted in spectral character inconsistent with the Martian deposits, and smaller proportions were only successful in the 63-90 and 125-180 μm grain sizes. The halite salt crusts on labradorite were also largely successful except for the 63-90 μm size fraction, whereas the flood basalt samples were only capable of emulating the desired spectral character in the case of the 125-180 and 250-355 μm size fractions.

The pyrite mixtures with both labradorite and flood basalt were incapable of reproducing the spectral character observed in CRISM ratio spectra, regardless of grain size or proportion. This is due to the rapid appearance of oxidation products in the acid-washed pyrite from the ≤15 minutes of time spent in open air that is necessary to produce homogeneous mixtures and collect NIR data. At this point, it is possible to discount pyrite as a possible component of the Martian deposits. This can bring us to the conclusion that these units are chloride-bearing, even if the proportion cannot be tightly constrained by this study. We are currently conducting a mid-IR spectral study using similar mixtures in an effort to place further constraints on both grain size and chloride abundance.

3. Effects of TES Training Regions and THEMIS Image Collection Conditions on Chloride Unit Spectral Variability

3.1 Introduction

Putative chloride-bearing deposits have been observed in the southern highlands of Mars. They are easily observable in Compact Reconnaissance Imaging Spectrometer for Mars (CRISM) data [*Glotch et al.*, 2010; *Jensen and Glotch*, 2011; see discussion in Chapter 2] and they have a distinctive aqua-blue color in Thermal Emission Imaging System (THEMIS) daytime mid-infrared band 9,6,4 decorrelation stretched (DCS) images [*Gillespie et al.*, 1986; *Osterloo et al.*, 2010; *Osterloo et al.*, 2008]. THEMIS daytime infrared data are often displayed as DCS images to allow for easy observation of compositional variability in highly correlated data by selecting 3 different wavelengths, assigning them to red, green and blue and then exaggerating the small differences in radiance. The distinctive color of these units in false-color mid-infrared THEMIS images is due to higher apparent emissivity between bands 3 (7.889 μm, 1267.62 cm^{-1}) and 8 (11.753 μm, 850.846 cm^{-1}) than the surrounding basaltic plains units, which display a minimum emissivity at band 5 (9.301 μm, 1075.09 cm^{-1}). These units display THEMIS spectra that have generally basaltic spectral character with a negative slope towards longer wavelengths (blue slope). The spectral slope is proposed to be the product of an incorrect assumption of isothermality and/or unit emissivity of the observed surface in the process of converting radiance to emissivity. Anisothermalities have not been found to exist where these materials are observed on the Martian surface and instead the spectral character is attributed to the presence of a material with non-unit emissivity, likely chloride salts [*Bandfield*, 2009; *Osterloo et al.*, 2008].

Through in-depth investigation of the spectral character of these deposits by remote sensing instruments and by laboratory studies at wavelengths ranging from visible to thermal

infrared, our understanding of the spectral properties of these proposed chloride-bearing units has been greatly enhanced [*Glotch et al.,* 2010; *Jensen and Glotch,* 2011; *Murchie et al.,* 2009; *Osterloo et al.,* 2010; *Osterloo et al.,* 2008; *Wray et al.,* 2009]. Whereas most of the deposits observed are smaller than a single Thermal Emission Spectrometer (TES) pixel (~3 km x ~6 km), the hyperspectral thermal infrared data analyzed over a wider wavelength range (~300 – 1300 cm^{-1} or ~33.33 – 7.70 μm) from the largest units reveal sloping emissivity spectra towards longer wavelengths with some basaltic character, similar to those viewed by THEMIS. This observation supports the conclusions drawn from lower spectral resolution (8 different wavelengths), higher spatial resolution (up to 80 m/ pixel) THEMIS data [*Osterloo et al.,* 2010; *Osterloo et al.,* 2008]. Studies of the high spectral and spatial resolution near infrared data from the Mars Reconnaissance Orbiter's (MRO) CRISM instrument reveal featureless red sloping spectra in the 1.1-2.5 μm wavelength range [*Glotch et al.,* 2010; *Murchie et al.,* 2009; *Wray et al.,* 2009]. As is discussed in Chapter 2, the red slope observed in this spectral range can be emulated in the laboratory by the admixture of halite with rocks/minerals such as flood basalt or labradorite [*Glotch et al.,* 2010; *Jensen and Glotch,* 2011].

Whereas numerous remote sensing instruments aboard several Mars missions have been used to fully characterize these units [*Glotch et al.,* 2010; *Murchie et al.,* 2009; *Osterloo et al.,* 2010; *Osterloo et al.,* 2008; *Wray et al.,* 2009], the effects on observed spectral character other than the surface mineralogy have not been fully investigated. This study sheds light on the effects of the atmospheric correction accuracy and data collection conditions on the overall spectral character observed in spectra extracted from corrected THEMIS images.

3.2 Data and Methods

THEMIS daytime 9,6,4 decorrelation stretched (DCS) images from the Martian southern highlands were evaluated in the Java Mission-planning and Analysis for Remote Sensing (JMARS) software for their distinct blue color in comparison with the surrounding terrain [*Weiss-Malik et al.*, 2005]. In regions containing these distinct units, corrected THEMIS daytime radiance images were downloaded using the THEMIS Processing Web Interface (THMPROC): http://thmproc.mars.asu.edu. THMPROC standard processing of desired images prior to downloading helps to remove artifacts in the data and correct partially for varying atmospheric components throughout an individual image. THMPROC standard processing includes corrections of temperature drifts and wobble within an image (UDDW), unslanting of the images (Rectify), line and row correlated noise removal (Deplaid) and an automated radiance correction that removes the radiance due to the atmospheric emission (Auto-radcorr).

The radiance observed by THEMIS can be described by the equation:

$$\mathrm{I}_{obs}(\nu) = \varepsilon(\nu) B[T_{surf}, \nu] e^{-\tau_0(\nu)/\mu} + \int_0^{\tau_0} \{B[T(p), \nu] e^{-\tau(\nu,p)/\mu} d\tau\}, \quad (1)$$

where $\mathrm{I}_{obs}(\nu)$ is the measured radiance. Equation 1 can be split into two terms; the first term is a proportional term accounting for atmospheric attenuation of surface radiance and the second is an additive term accounting for emissions due to the atmosphere. In the proportional term, $\varepsilon(\nu)$ is the surface emissivity; $B[T_{surf}, \nu]$ is the blackbody radiance as a function of surface temperature (T_{surf}) and frequency (ν); and $e^{-\tau_0(\nu)/\mu}$ represents atmospheric attenuation of the surface radiance, where $\tau_0(\nu)$ is the opacity at the surface for a given frequency and μ is the cosine of the emission angle. In the additive term (integral), $B[T(p), \nu]$ is the blackbody radiance as a function of temperature (proportional to atmospheric pressure) and frequency; $\tau(\nu, p)$ is the normal opacity profile as a function of frequency and pressure; and μ is the cosine of the

emission angle. The integral is taken from the opacity at the spacecraft (0) to the surface opacity (τ_0) [*Bandfield et al.*, 2004]. In the two step process of removing the atmospheric effects on radiance in THEMIS images, this equation can be simplified to:

$$I_{obs}(\nu, n) = A(\nu)B[T_{surf}, \nu, n] + C(\nu). \quad (2)$$

In Equation 2, $I_{obs}(\nu, n)$ is the radiance observed at a given spectral band (ν) and pixel (n); $A(\nu)$ represents surface emissivity and atmospheric attenuation; $B[T_{surf}, \nu, n]$ is the Planck radiance at the kinetic temperature of the surface (T_{surf}) for a given spectral band and pixel; and $C(\nu)$ is the atmospheric emission term [*Bandfield et al.*, 2004]. $C(\nu)$ is removed using an automated radiance correction (Auto-radcorr) developed by the THEMIS team,

$$\tau_0(\nu)/\mu = -\ln\left(\frac{I_{obs}(\nu,n)}{\{B[T_{surf},\nu,n]\cdot\varepsilon(\nu)\}}\right). \quad (3)$$

To retrieve the desired quantity, surface emissivity, the contribution from atmospheric attenuation must be determined. This is determined by finding an area within the image with emissivity that is considered known and using Eq. 3 to retrieve the atmospheric contribution. The atmospheric contribution is then assumed to be the same over the area of interest and Eq. 3 is used to retrieve surface radiance for the area of interest

The region of known emissivity is determined using TES data. The surface emissivity is extracted from TES pixels overlapping a spectrally homogenous region, called a TES training region, within the THEMIS DCS image and used to calculate the atmospheric attenuation which can then be removed from all pixels throughout the THEMIS radiance image [*Bandfield et al.*, 2004]. A minimum of nine TES pixels from the same OCK (orbit counter keeper) are used for the TES training region to ensure that a large area (~10 x 10 km) of the THEMIS image is covered. The TES training region pixels are selected using the JMARS software with many constraints enacted to ensure spectra are of high quality, from a warm surface and with a clear

atmosphere. The constraints used during TES training region selection include pixels with data from single length scans of 10 cm^{-1} spacing (scan_len=1), with derived target temperatures of 250 – 340 K (target_temp=250-340), a lack of phase inversions (phase_inversion=0), at low risk of algor phase inversions (algor_risk=0), no image motion compensation (pnt_imc=0), separate spectra transmitted to Earth for all six detectors (det_mask=7), spectra from all detectors are used (spectral_mask=0), data collected at emission angles of 0-5º (emission=0-5), with the smallest effect of atmospheric opacity (atm_opacity_rating=0), minimal atmospheric water ice clouds (tot_ice=0-0.04) and OCK values of 1583-7000 (ock=1583-7000). Only TES spectra from pixels that meet all of these constraints are used to calculate and remove the atmospheric attenuation component from the THEMIS image radiance data.

Once radiance data are fully corrected, they are converted to emissivity, resulting in a surface emissivity image that is theoretically free of artifacts due to atmospheric emission. Regions in the image displaying the characteristic aqua color of a chloride unit in 9,6,4 DCS images with pixel areas larger than 5x5 pixels (~500 m^2) are selected and spectra are averaged over the defined pixel area. A proximate background unit from a basaltic plains region and the TES training region are also selected and spectra are averaged over the unit area for comparison to the chloride unit.

There are a few sources of error in the process of correcting and converting radiance data to emissivity data. Inaccurate TES surface emissivity data used to estimate the atmospheric attenuation term can result in errors in corrected THEMIS data. The accuracy of the TES surface emissivity depends on 1) the atmospheric contribution in the data and 2) the spectral library used in data analysis. The original standard spectral library used for analyzing TES data contains spectra of more than 150 rock-forming minerals, not including many phyllosilicates, high-Si

minerals and zeolites [*Christensen et al.*, 2000]. The presence of spatially variable atmospheric water ice clouds in any region of the image will also introduce error into the THEMIS surface emissivity derivation. Spectra of water ice in the wavelength range of the THEMIS instrument have an emissivity maxima at band 5 (9.35μm, 1075.09 cm^{-1}) and slopes downwards towards longer wavelengths. A large difference in altitude between the TES training region and the area(s) of interest could also produce errors in the THEMIS surface emissivity.

It is important to understand the influence of components other than the mineralogy of the surface on spectral character of putative chloride-bearing deposits in mid-infrared THEMIS data. In regions with multiple THEMIS daytime IR images overlapping a chloride unit, data were extracted from these images using identical TES training regions for the manual atmospheric correction to understand the effects of data collection conditions on spectral character. Possible variation due to the selection of TES training region pixels for the atmospheric correction was also analyzed by processing the images with TES training regions from different areas within a single THEMIS image. In order to observe the overall effects of the TES training region used in the atmospheric correction of THEMIS images, properties of the TES training region are compared to the spectral slope of the defined chloride unit. The chloride unit spectral slopes were determined by subtracting the emissivity of band 8 (11.753 μm, 850.846 cm^{-1}) from the emissivity of band 3 (7.889 μm, 1267.62 cm^{-1}) and dividing by the change in wavelength between the two band centers (3.86 μm, 416.774 cm^{-1}). The difference in surface temperature between the training region and the chloride unit (T_{train}-$T_{chloride}$) and the minimum emissivity of the training region, observed at band 5, were properties of particular interest. The temperatures of the chloride unit and training region units were extracted by averaging the same pixel regions used for the mid-infrared data from the surface temperature files for the same THEMIS image.

A total of 109 images containing chloride units located from -51.4 to -1.809 ºN latitude and 140-240 ºE and 320-350 ºE longitude have been fully analyzed to observe spectral variability. These 109 THEMIS images have minimum surface temperatures ranging from 167.928 to 258.27 K and maximum surface temperatures ranging from 245.014 to 300.638 K. THEMIS observation parameters for the images include solar longitudes ranging from 3.36º to 359.23º (essentially covering the full Martian year) and solar times ranging from 14.74 to 17.75. Of these, 57 images have been processed using more than one TES training region for the atmospheric correction. In 10 different cases, overlapping THEMIS images containing chloride unit(s) have been analyzed using the same TES training region for the removal of the atmospheric emission component.

3.3 Results

In order to observe the spectral variability of the chloride unit due to the choice of a TES training region, a series of plots of the chloride unit spectral slope between bands 3 and 8 versus characteristics of the TES training region have been produced.

Figure 3-1 shows the variability in chloride unit spectral slope due to the TES training region's minimum emissivity at band 5. In this case, if multiple chloride units were defined for a given TES atmospheric correction, the chloride unit spectral slopes were averaged so that there is one chloride unit spectral slope for each TES training region. A weak negative correlation (R^2= 0.1997) exists between TES training region minimum emissivity and the slope of the chloride unit spectra.

Figure 3-2 shows the relationship between the chloride unit spectral slope and the TES training region temperature. The TES training region temperature is derived from the THEMIS

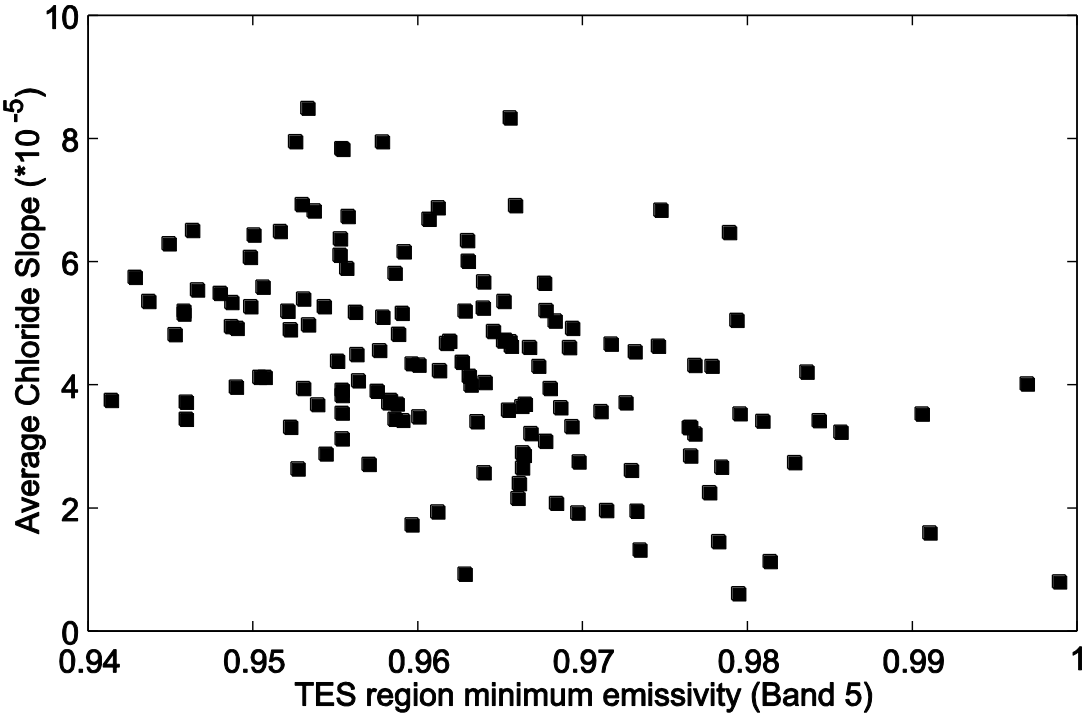

Figure 3- 1. Plot of the averaged chloride unit spectral slopes from each THEMIS image and each atmospheric correction versus minimum THEMIS emissivity values for the TES training regions (band 5) for all THEMIS images analyzed in this study.

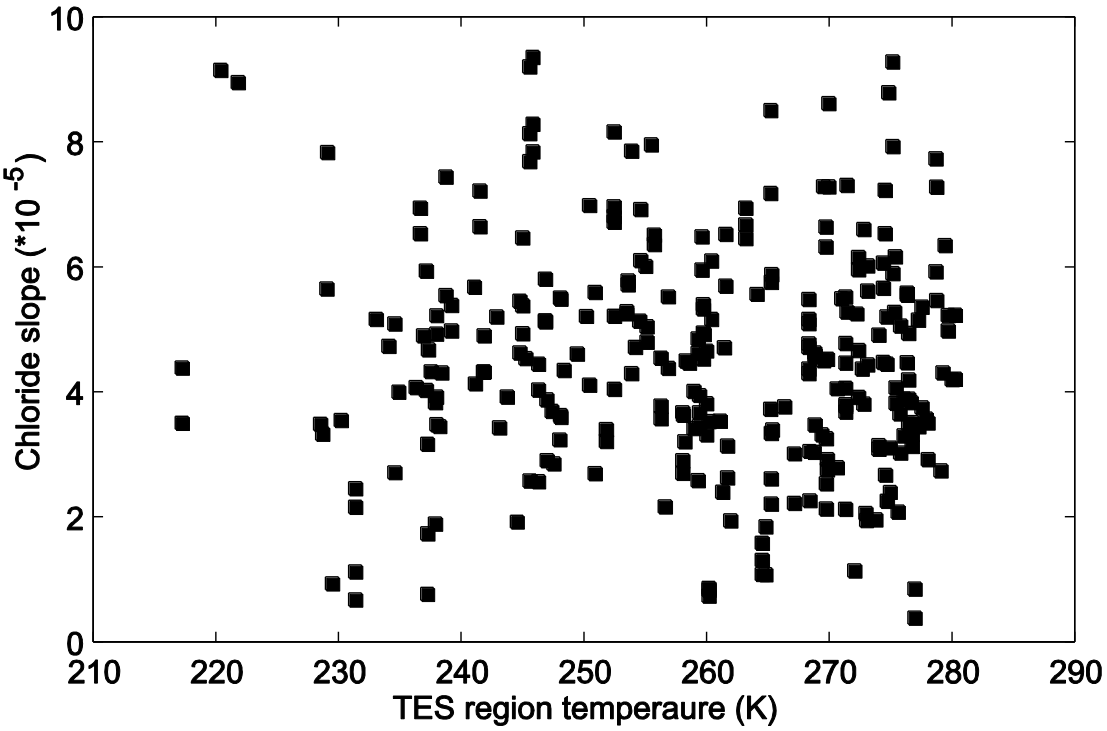

Figure 3- 2. Plot of the spectral slope between bands 3 and 8 for each chloride unit and each manual atmospheric correction versus the surface temperature of the TES training region derived from the THEMIS surface temperature data for each image.

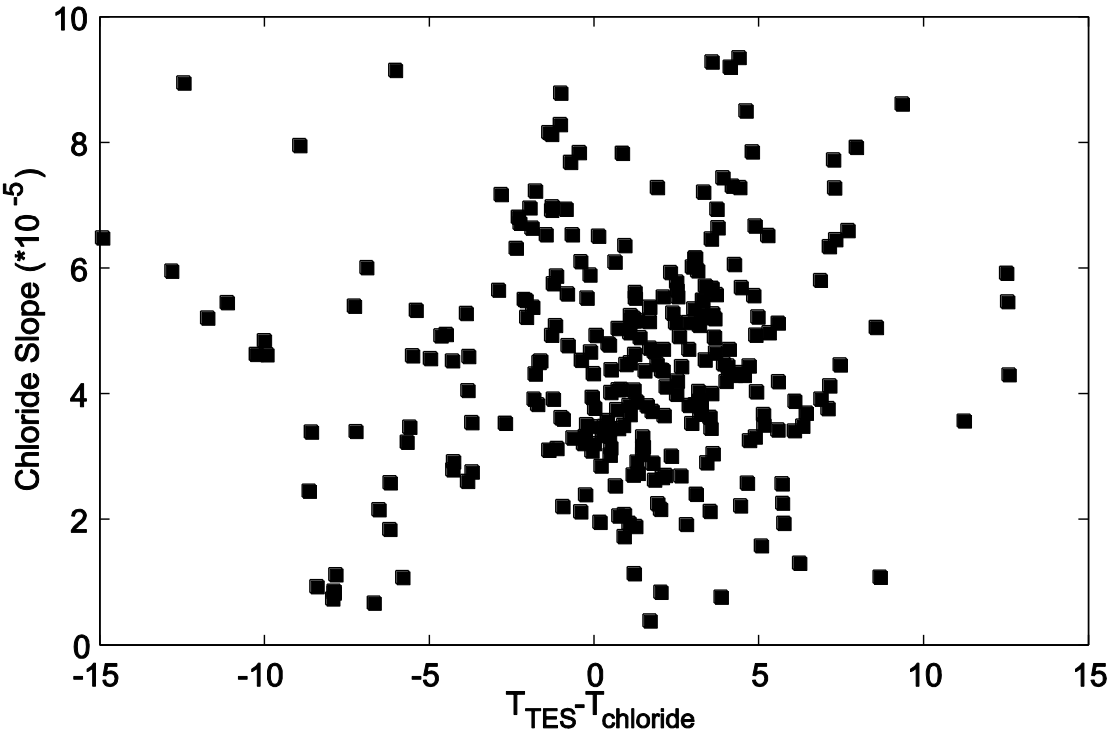

Figure 3- 3. Plot of the slope between bands 3 and 8 for each chloride unit and manual atmospheric correction versus the difference in the surface temperature between the TES training region and the chloride unit. The surface temperatures are derived from the THEMIS surface temperature data for each image.

image surface temperature data. Though there is extensive variability in chloride unit spectral slope versus TES training region temperature, there is no relationship observed.

In Figure 3-3, the relationship between the chloride unit spectral slope and the difference in surface temperature between the chloride-bearing unit and the TES training region is displayed. Whereas there is extensive variation in the plotted data, there is no correlation observed between the chloride unit spectral slope and the difference in surface temperature between the chloride unit and the TES training region.

3.3.1 Chloride spectral variation due to TES training region selection

In order to display the variation in spectral character induced by the selection of the TES training region used in the manual atmospheric correction, two examples have been chosen; one that displays chloride unit spectral slope variability due to changes in the TES training region used in the atmospheric and one that shows little change in the chloride unit's spectral character despite a large change in the location of the TES training region within the THEMIS image. For each example, a background unit of basaltic composition within the image has also been selected to show how the basaltic spectral character is changed by TES training region selection used in removal of the atmospheric attenuation.

In the case of THEMIS image I17393002, 3 different TES training regions within the image were used for the atmospheric correction. TES training region information is summarized in Table 3-1. The locations of the TES training regions, spectrally defined chloride units and background units can be observed in Figure 3-4. The three spectrally defined chloride units are disbursed throughout the THEMIS image from over 200 km north of the northernmost TES training region to ~15 km from the middle TES training region. The northern TES training region yields chloride unit spectral slopes that are almost twice the magnitude of the chloride

unit spectral slopes observed for the two southern TES training regions (Figure 3-5). An increased slope is also observed between bands 3 and 8 in the background and TES training region spectra in comparison with the resulting overall spectral slope where the other two atmospheric correction regions are used. Regardless of which TES training region is used, the southern chloride unit consistently has the largest slope in emissivity between bands 3 and 8 and the middle chloride unit has the smallest change in emissivity in this wavelength region. Whereas the middle and southern TES training regions yield similar chloride unit spectral slopes, the southern TES training region yields chloride unit spectra with increased basaltic character, observed by local emissivity minima at band 5. This increased basaltic character is also enhanced in the background unit where the southern TES training region is used in the atmospheric correction in comparison with where the middle TES training region is used. The surface temperature is highest for the middle TES training region and lowest for the southern TES training region. In summary, the changes in chloride spectral slope cannot be directly attributed to the TES surface temperature, minimum emissivity or location with respect to the chloride units.

Table 3- 1. I17393002 TES training region information

TES region	TES region location	TES min. emissivity	T_{TES} (K)[a]	Relative chloride location	Chloride slope ($*10^{-5}$)
1	194.13 - 194.35E, -32.26 - -32.13N	0.96	268.3	Northern	4.8
				Middle	4.4
				Southern	5.5
2	193.73 - 193.98E, -36.375 - -36.175N	0.95	269.7	Northern	2.5
				Middle	2.1
				Southern	3.3
3	193.18 - 193.43E, -39.96 - -39.75N	0.96	265.2	Northern	2.6
				Middle	2.2
				Southern	3.3

[a] The surface temperature of the TES training region derived from the THEMIS surface temperature data.

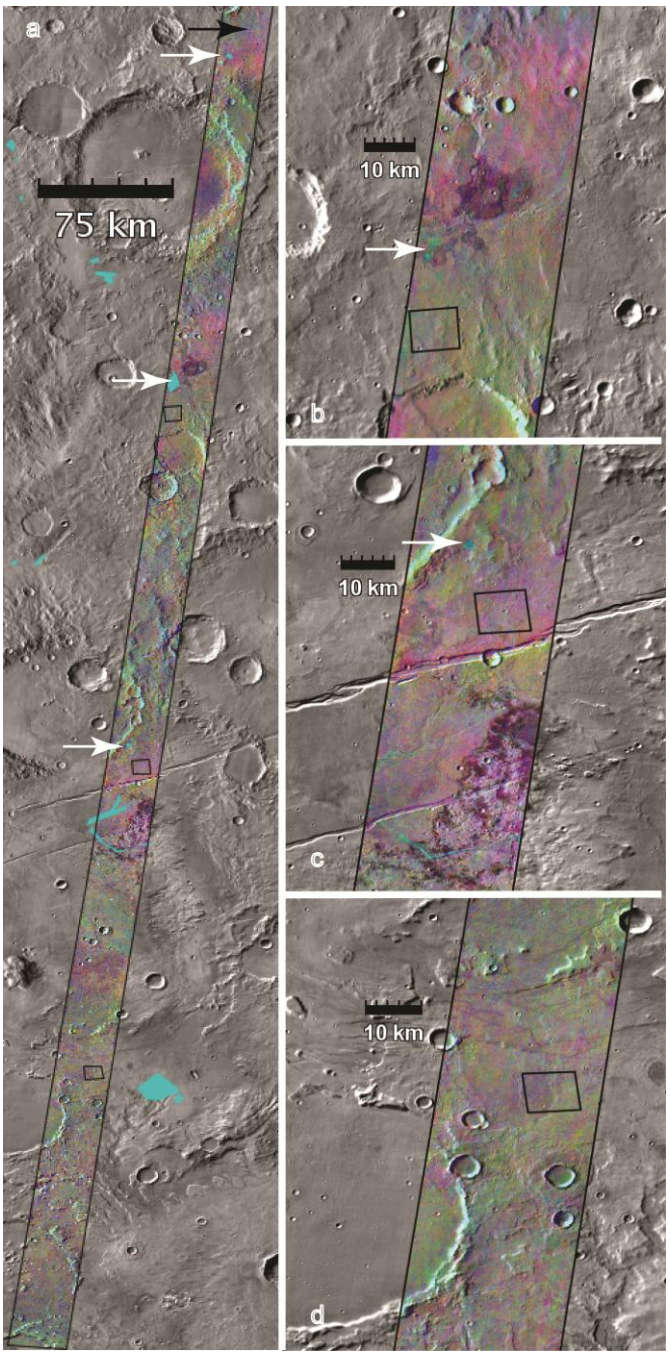

Figure 3- 4. THEMIS daytime IR DCS image I17393002 a) where bands 9, 6, and 4 are red, green and blue (respectively) overlaid on the THEMIS Day IR 100m Global Mosaic with the Osterloo et al, 2010 Chloride Survey shape file indicating the locations of chloride deposits. Boxes show where the TES training regions used in the atmospheric correction are located, white arrows represent the defined chloride units and black arrows indicate background unit. The image is centered at 193.5E, -35.25N. b) Image centered at 194.4E, -31.75 displaying the northernmost TES training region with a proximal chloride unit (indicated by the white arrow). c) Image centered at 193.75E, -36.5N displaying the central TES training region and proximal chloride unit (depicted by white arrow). d) Image centered at 193E, -40N displaying the southernmost TES training region.

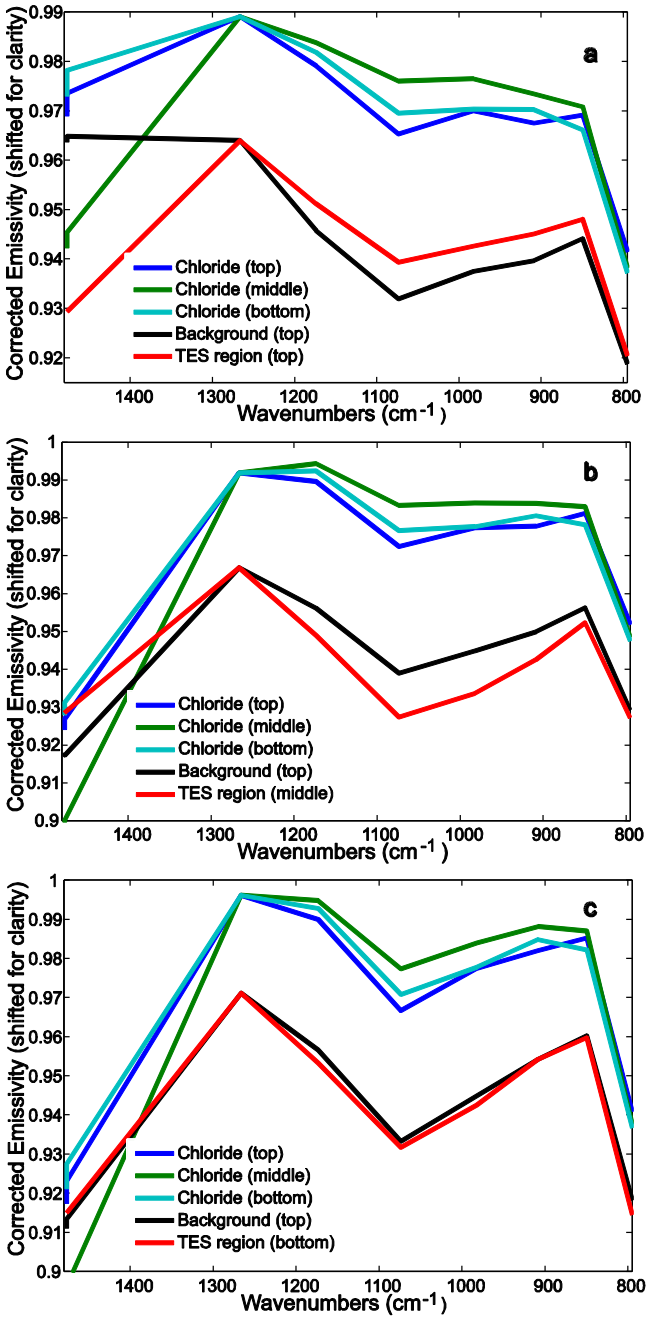

Figure 3- 5. Plots of the THEMIS image I17393002 spectra averaged over the regions depicted in Figure 3-4 using a) the northern TES training region for the atmospheric correction (Figure 3-4b), b) the central TES training region for the atmospheric correction (Figure 3-4c), and c) the southern TES training region for the atmospheric correction (Figure 3-4d). The emissivity of background and TES training region spectra have been shifted for clarity in all plots (-.025).

Table 3- 2. I17455004 TES training region information

TES region	TES region location	TES min. emissivity	T_{TES} (K)[a]	Relative chloride location	Chloride slope ($*10^{-5}$)
1	205.77 - 206.02E, -31.88 - -31.65N	0.97	268.3	Northern	4.7
				Middle	5.1
				Southern	4.3
2	203.9 - 204.17E, -43.73 - -43.53N	0.98	259.7	Northern	4.9
				Middle	5.3
				Southern	4.5

[a]The surface temperature of the TES training region derived from the THEMIS surface temperature data.

Where THEMIS image I17455004 was analyzed using two different TES training regions for the atmospheric attenuation correction from areas of the THEMIS image that are over 500 km apart (Figure 3-6), little variation is observed in the resulting chloride unit spectral slopes. TES training region information and resulting chloride unit spectral slopes can be observed in Table 3-2 and spectral plots are displayed in Figure 3-7. The chloride unit spectra resulting from use of the southern TES training region in the removal of the atmospheric attenuation do have an increased basaltic character in comparison with the derived spectra from using the northern TES training region. Even though the TES training region locations, minimum emissivities and surface temperatures are quite different for the two TES training regions, the chloride unit spectral slopes are not extremely different.

3.3.2 Spectral variation due to changes in THEMIS observation conditions

In addition to the effects of TES training regions on chloride unit spectral character, spectral changes induced by THEMIS observation conditions are also of interest. Multiple THEMIS images overlapping a chloride unit were examined with atmospheric attenuation corrections conducted using the same TES training region to understand the effects of different observation conditions on spectral character. Two different examples are discussed here.

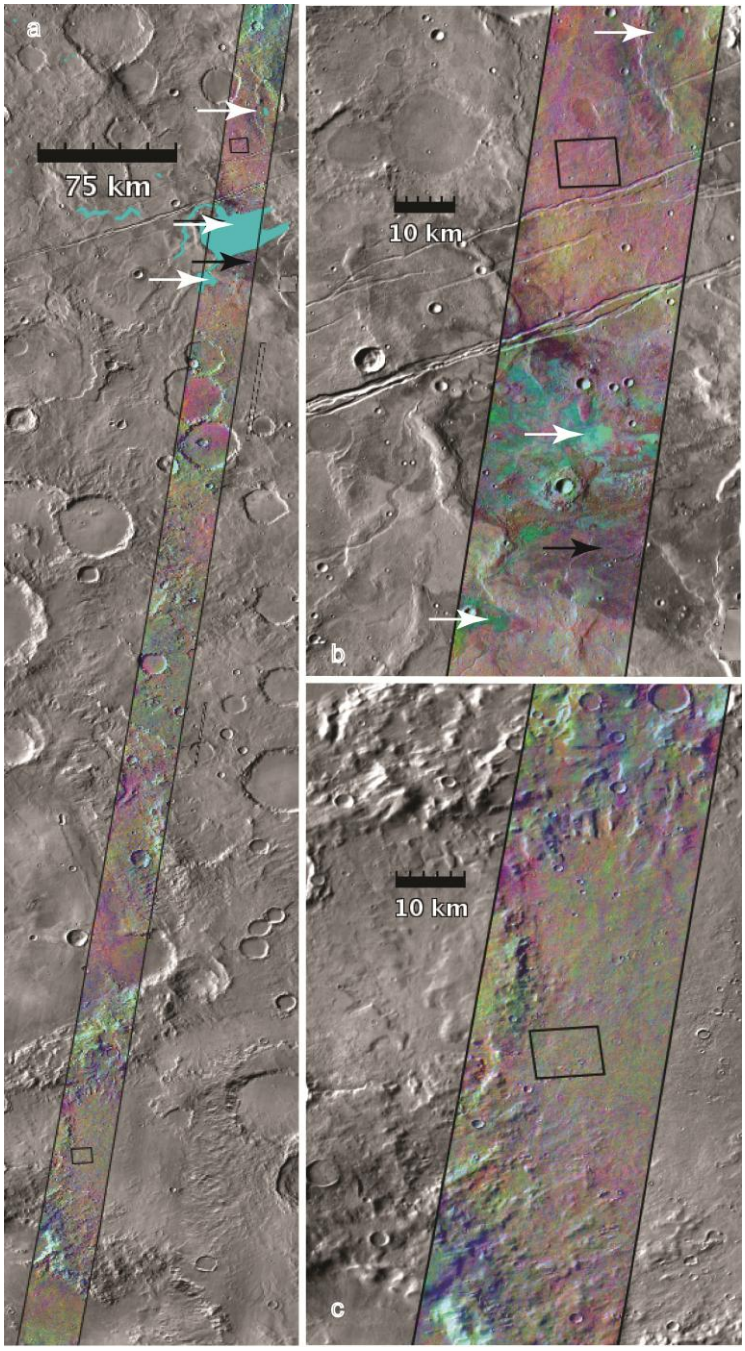

Figure 3- 6. THEMIS daytime IR DCS image I17455004 a) where bands 9, 6, and 4 are red, green and blue (respectively) overlain on the THEMIS Day IR 100m Global Mosaic with the Osterloo et al, 2010 Chloride Survey shape file depicting the locations of chloride deposits. Boxes show where the TES training regions used in the atmospheric correction are located, white arrows represent the defined chloride units and black arrows indicate background units. The image is centered at 204.5E, -38N. b) Image centered at 205.75E, -32.35N displaying the northernmost TES training region with a proximal chloride unit (indicated by the white arrow). c) Image centered at 203.9E, -43.5N displaying the southern TES training region.

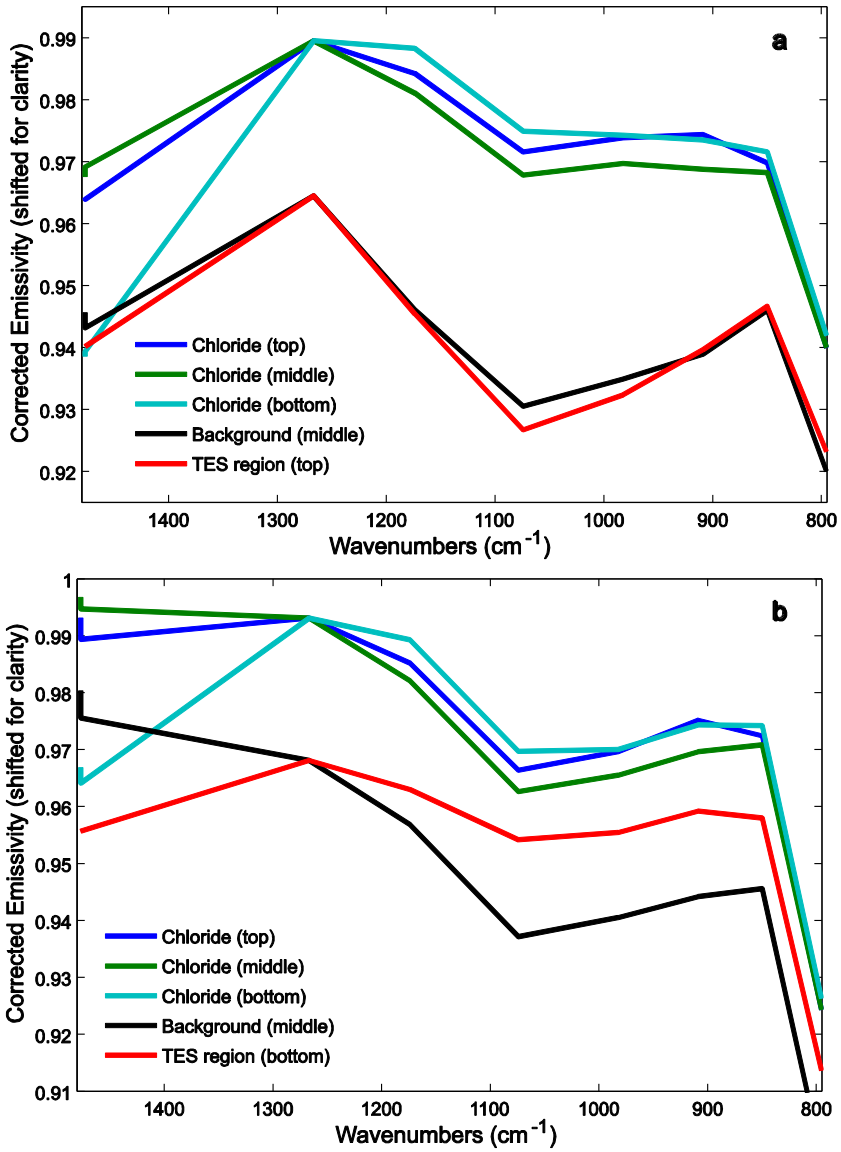

Figure 3- 7. Plots of the THEMIS image I17455004 spectra averaged over the regions depicted in Figure 3-6 using a) the northern TES training region for the atmospheric correction (Figure 3-6b) and b) the southern TES training region for the atmospheric correction (Figure 3-6c). The emissivity of the background and TES training region spectra have been shifted for clarity for both plots (-.025).

Table 3- 3. I09780002 overlapping image information

Image ID	Relative chloride location	min. T_{surf} (K)[a]	max. T_{surf} (K)[b]	L_s[c]	Solar time	Chloride slope ($*10^{-5}$)	T_{TES} (K)[d]
I09780002	Northern	204.69	270.35	356.46	16.19	4.1	246.0
	Southern					5.2	
I17455004	Northern	230.94	288.29	327.29	16.07	6.1	268.1
	Southern					5.6	
I18990003	Northern	167.928	245.364	30.64382	16.618	4.4	217.2
	Southern					3.5	
I17143004	Northern	241.97	292.07	312.73	16.11	5.5	274.4
	Southern					4.5	

[a] The minimum surface temperature within the THEMIS image. [b] The maximum surface temperature within the THEMIS image. [c] The solar longitude at the time that the THEMIS image was collected. [d] The surface temperature of the TES training region derived from the THEMIS image surface temperature data.

Figure 3-8 displays the first example which includes four overlapping THEMIS images, where a set of chloride units is located at the bottom right of THEMIS image I09780002, the upper middle of images I18990003 and I17455004 and the top left of I17143004. THEMIS overlapping image information and chloride unit spectral slopes are summarized in Table 3-3.

Images were collected in the late afternoon between late northern hemisphere winter and spring. The spectral differences between these four images can be observed in Figure 3-9. The TES training region spectra are identical in all four images because they are the source of the atmospheric correction of the image data. A difference in overall emissivity of ~.01 between the two chloride units is observed in I09780002, whereas the other three images yield chloride unit spectra of similar overall emissivity. All chloride unit spectra again have a basaltic component in their spectra, with the defined chloride unit spectra from images I17455004 and I17134004 having the smallest basaltic input. The most noticeably different chloride unit spectra are observed in image I18990003, where the chloride unit spectra do not overlap the TES training region spectrum at 1174.85 cm^{-1} as is observed in the three other images. An interesting

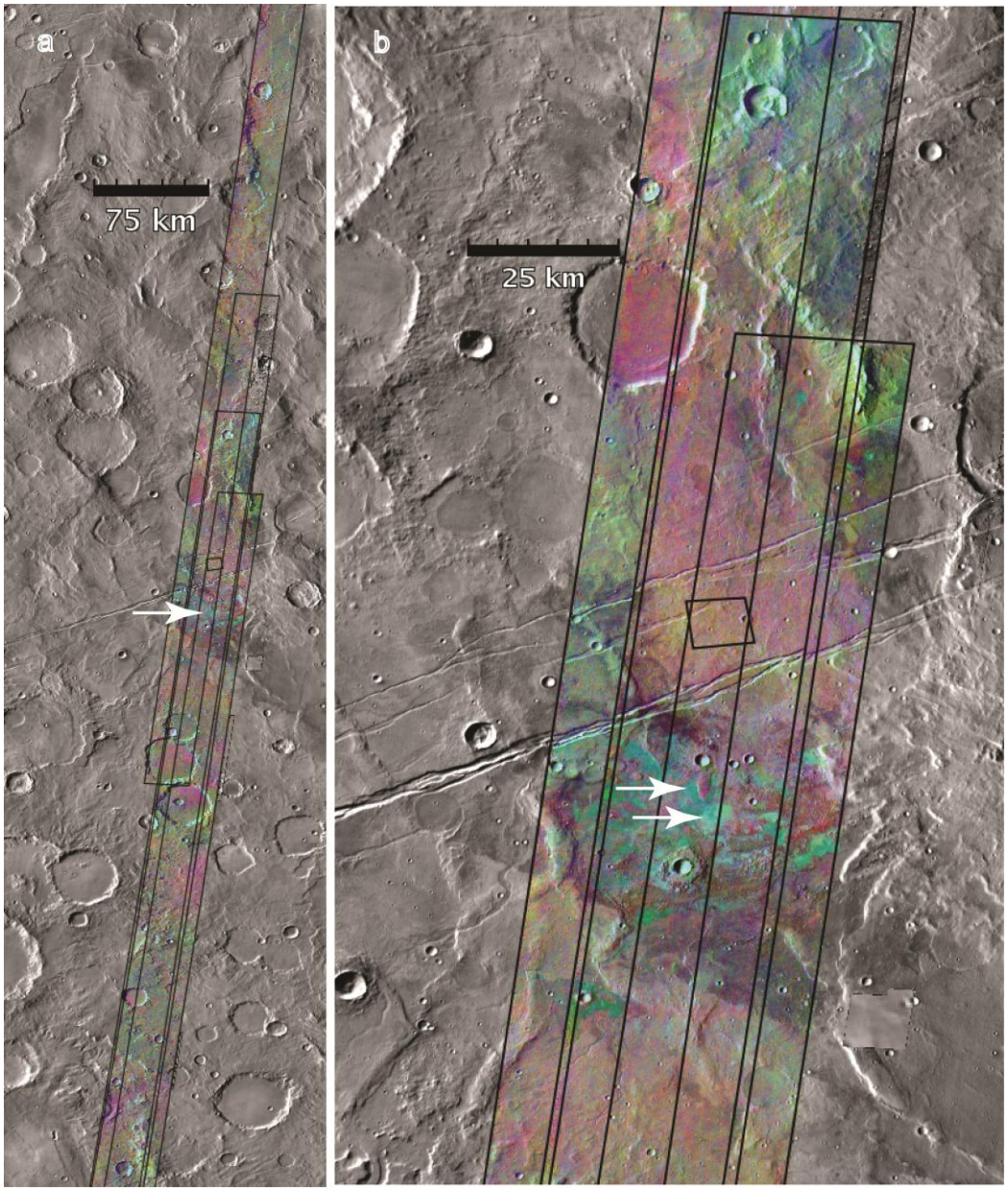

Figure 3- 8. THEMIS daytime IR images I09780002, I17455004, I18990003, and I17143004 (from left to right) rendered as band 9, 6, 4 DCS images a) overlain onto the THEMIS Day IR 100m Global Mosaic. The black box indicates the TES training region used for the atmospheric correction of all 4 THEMIS images and a white arrow indicates the location of the chloride units analyzed within the overlapping region. The image is centered at 205.5E, -32.5N. b) A close up view of the overlapping THEMIS region with white arrows indicating the chloride units used for spectral analysis. The image is centered at 206E, -32N.

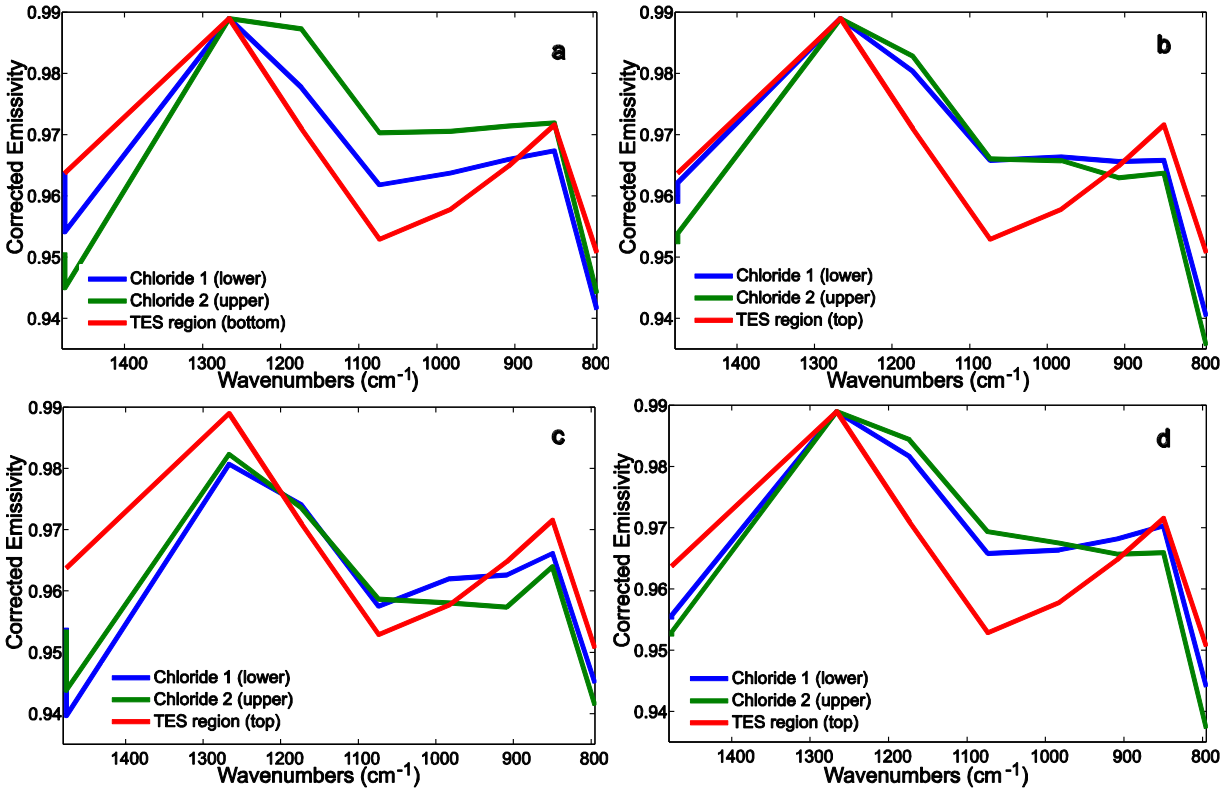

Figure 3- 9. Averaged spectra of THEMIS pixels for areas indicated in Figure 3-8 for THEMIS images a) I09780002, b) I17455004, c) I18990003, and d) I17143004.

observation concerning the chloride unit spectral slopes is that in most cases the lower chloride unit has a larger slope (II17455004, I18990003 and I17143004), whereas in the case of I09780002 the upper chloride unit has a greater change in emissivity between bands 3 and 8. This cannot be explained by the observation conditions because I09780002 does not have extreme surface temperatures, solar longitude or solar time in comparison with the other images.

Table 3- 4. I07821003 overlapping THEMIS information

Image ID	min. T_{surf} (K)[a]	max. T_{surf} (K)[b]	L_s[c]	Solar time	Chloride slope ($*10^{-5}$)	T_{TES} (K)[d]
I07821003	235.12	294.1	263.62	16.79	4.6	270.5
I06710002	222.21	272.99	206.33	17.34	4.6	248.4
I23296003	208.77	260.7	201.29	17.74	4.4	238.1

[a] The minimum surface temperature within the THEMIS image. [b] The maximum surface temperature within the THEMIS image. [c] The solar longitude at the time that the THEMIS image was collected. [d] The surface temperature of the TES training region derived from the THEMIS image surface temperature data

The chloride unit in the second example is located in the lower right of image I07821003, the middle right of I06710002 and the lower left of I23296003 (Figure 3-10). THEMIS overlapping image information and chloride unit spectral slopes are summarized in Table 3-4.

All images were collected in the late afternoon. Data collection conditions vary from northern hemisphere autumn to just before the winter solstice indicating spring to summer conditions in the region we are examining. Temperatures of the images follow this change in season closely with image I23296003's data collected close to the northern hemisphere autumnal equinox with the coldest surface temperatures (208.77 – 260.77K), image I06710002 collected in between and with intermediate temperatures (221.21 – 272.99K) and image I07821003 collected just before the northern hemisphere winter solstice and having the highest temperatures (235.12 – 294.1K). The chloride unit spectral slope does not show large variation between images and

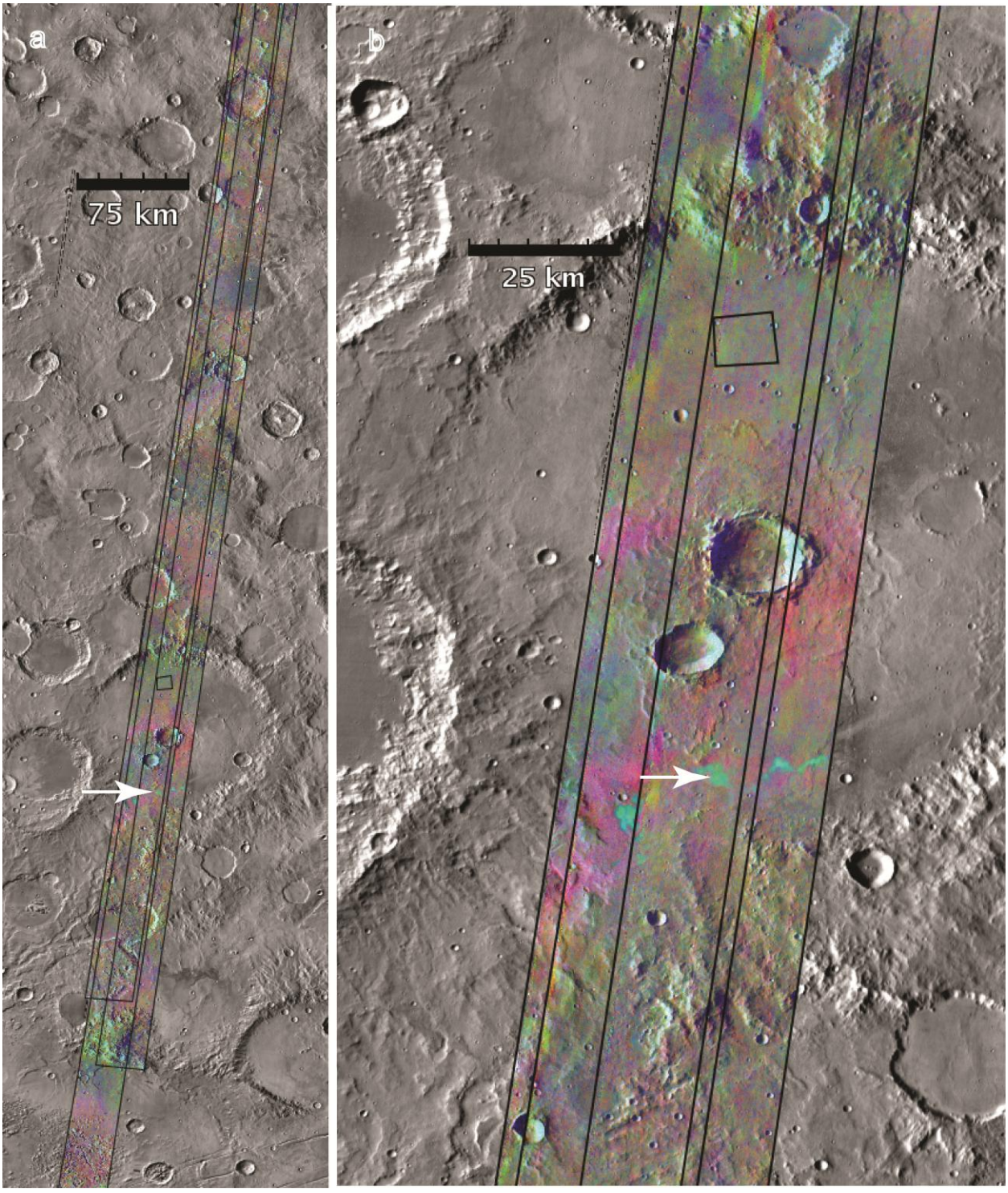

Figure 3- 10. THEMIS daytime IR band 9, 6, 4 DCS images I07821003, I06710002, I23296003 (from left to right) a) overlain on the THEMIS day IR 100m Global Mosaic with the TES training region indicated by the black box and the chloride unit is identified by the white arrow. Image is centered at 191E, -29.5N. b) A closer view of the overlapping region of the THEMIS images with the TES training region indicated by the black box and the defined chloride unit indicated by the white arrow. Image is centered at 190.5E, -31.5N.

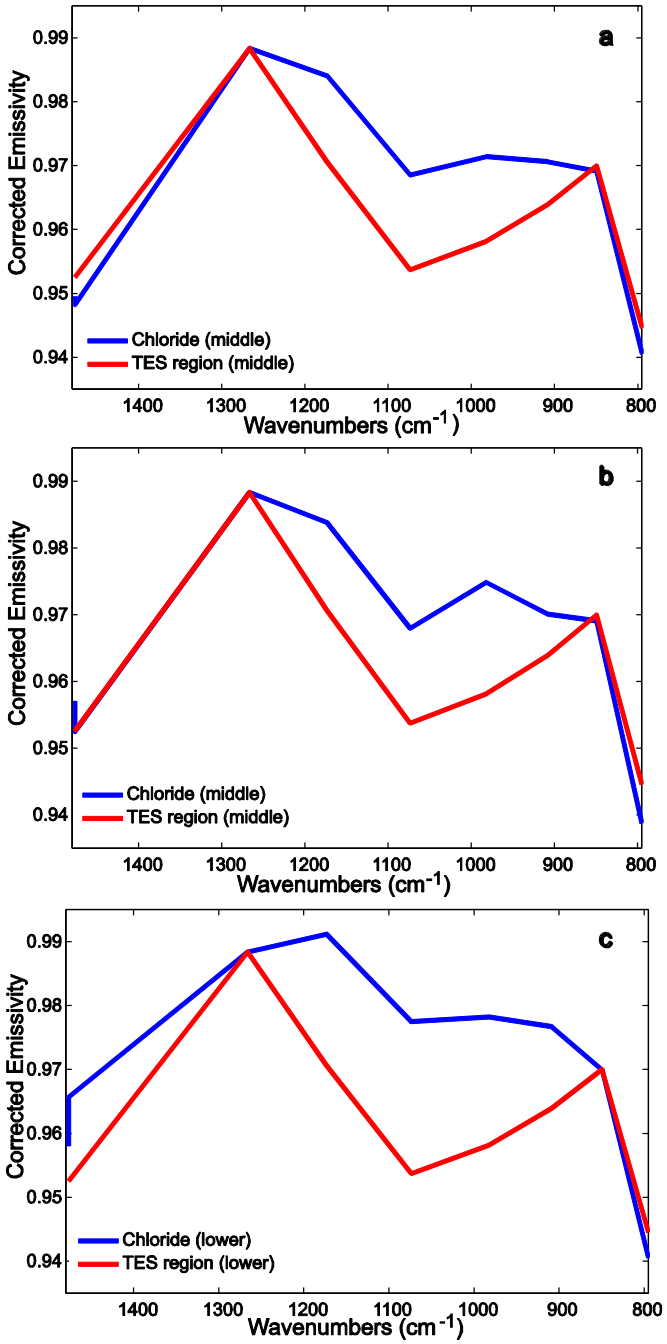

Figure 3- 11. Plots of the averaged spectra for the THEMIS pixel regions depicted in Figure 3-10 for THEMIS image a) I07821003, b) I06710002 and c) I23296003.

the basaltic influence on the chloride unit spectra appears similar (Figure 3-11). In this example, spectral variation does not correlate with seasonal or temperature variations.

3.4 Discussion

Plotting chloride unit spectral slope versus TES training region characteristics reveals only a weak correlation with TES training region minimum emissivity values. The observation that lower minimum emissivities result in larger chloride unit spectral slopes could be an indication that more basaltic TES training regions result in better chloride unit spectra. TES training region temperatures and the difference between TES training region temperatures and chloride unit temperatures show no relationship with chloride unit spectral slope based on this study's observations.

The use of different TES training regions to correct the emissivity of the same THEMIS image can result in slope alterations as well as variations in the basaltic imprint on the chloride unit spectral character. Unfortunately, changes in chloride unit spectral character cannot be directly connected with TES training region characteristics examined in this study; relative location, surface temperatures derived from the THEMIS image or minimum emissivity values. In the examples of THEMIS images I17393002 and I17455004, the changes in the chloride unit spectral slopes resulting from different TES training regions appear to be pseudo-proportional (the relative magnitudes of the slopes does not change, e.g. the southern chloride unit in I17393002 has the largest slope, followed by the northern chloride unit and the middle chloride unit spectral slope is smallest). The differences in the minimum emissivity of the chloride unit spectra of the two southern TES training region plots for THEMIS image I17393002 (Figure 3-5c and d) display that chloride unit spectral slope similarities do not indicate similar spectral character. An interesting observation from the southern TES training region of I17455004

(Figure 3-7b) is that the chloride unit spectral shape may have a basaltic character even where the TES training region spectrum lacks a notable minimum emissivity near band 5 and is practically featureless. Chloride unit spectral slope variations due to the use of different TES training regions to correct the emissivity values of a single THEMIS image appear to be greater than the variation observed between overlapping THEMIS images examined using the same TES training region.

THEMIS images overlapping chloride unit(s) corrected using the same TES training region reveal chloride unit spectral character that cannot be explained by differences in the Martian season, time of day or surface temperature ranges within the image area at the time of THEMIS image data acquisition. In the two examples used, surface temperature values correlated nicely with the seasonal temperature variations for each THEMIS image. Chloride unit spectral slope did not vary corresponding to these temperature or seasonal variations. In contrast with the multiple TES training region examples, changes in chloride unit spectral slope between overlapping THEMIS images do not stay in similar proportion (Table 3-3). In the first overlapping THEMIS image example, the southern chloride unit has a larger spectral slope for image I09780002 whereas in the other three images the northern chloride unit has a larger spectral slope. Whereas the differences in chloride spectral slope due to TES training region selection appear to be larger, the spectral slope variations observed in overlapping THEMIS images are unpredictable.

Due to the observed variability where different TES training regions are used for the atmospheric correction and in overlapping THEMIS images using the same TES training region, it is not currently possible to analyze the THEMIS spectral character of chloride units and draw conclusions about possible compositions or abundances. Until spectral variability due to the

atmospheric correction and data collection conditions can be better characterized and accounted for, the mineralogical variability of chloride-bearing deposits on the Martian surface cannot be ascertained using THEMIS data.

3.4.1 Atmospheric Modeling

In order to understand the effect that the TES training region and magnitude of the atmospheric contribution have on the atmospheric correction and resulting spectral character, some simple modeling was conducted. THEMIS image I17455004 was used to observe the variations in chloride unit spectral shape due to changes in the composition of the TES training region and the magnitude of the derived atmospheric contribution.

First, the contrast of the TES training region averaged spectrum and derived atmospheric component spectrum from I17455004 were both artificially increased and decreased. The resulting chloride unit spectral shapes display varying basaltic signatures (local emissivity minimum at band 5), with exaggeration of the TES training region spectrum resulting in an increased basaltic signature in the chloride unit spectral shape and muting of the TES training region spectrum resulting in flattening of the chloride unit spectrum (Figure 3-12a, b). Altering the contrast of the atmospheric contribution derived from the TES training region averaged spectrum (Figure 3-12c, d) resulted in convex chloride unit spectra when the atmospheric component is exaggerated and chloride unit spectra that have an increased basaltic component when the atmospheric component is understated.

Modeled TES training region compositions were constructed to understand the effects of the atmospheric correction on corrected surface emissivity values. This allows a complete understanding of effects of the TES training region surface composition on the resulting surface emissivity spectra. In the two models constructed, the surface composition is shifted from basalt

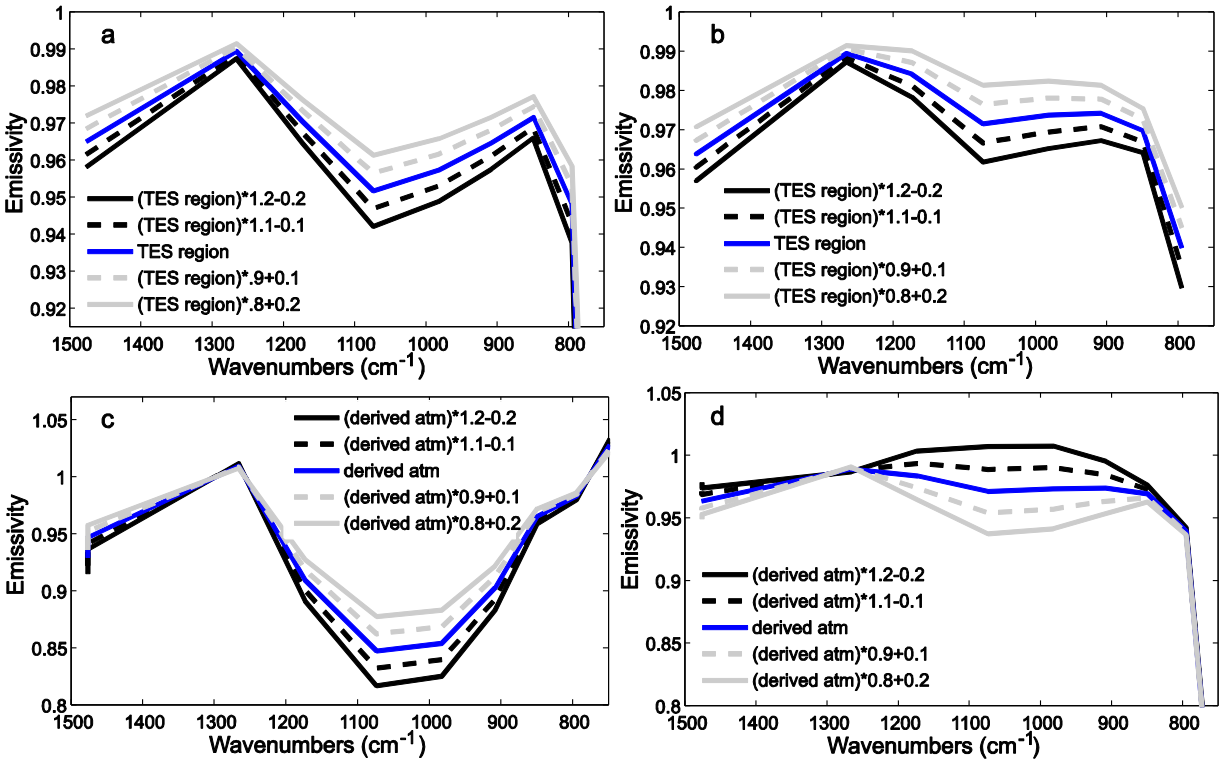

Figure 3- 12. Spectral modeling using the TES training region spectrum and derived atmospheric contribution spectrum from THEMIS image I17455004. a) Altered magnitude of the TES training region and b) resulting chloride spectral shape. c) Altered magnitude of the atmospheric contribution and d) resulting chloride spectral shape.

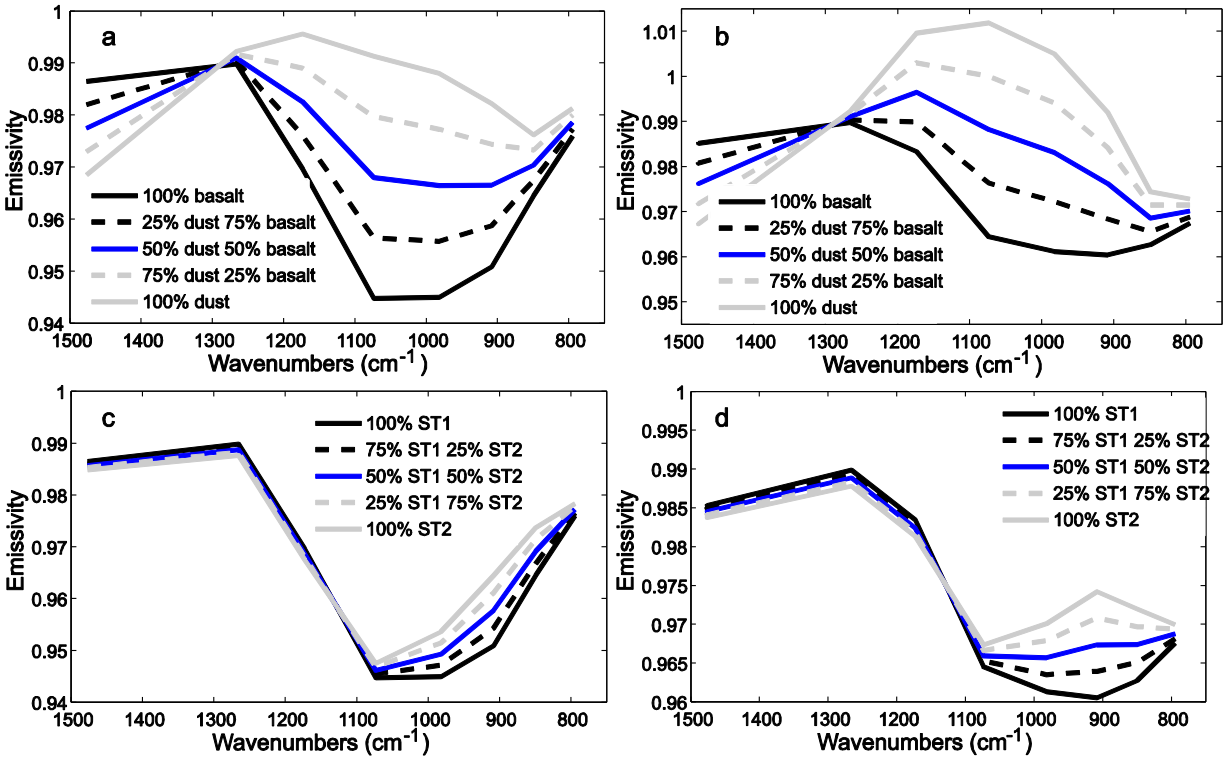

Figure 3- 13. Spectral modeling of the effect of the TES training region composition on the resulting chloride unit spectral shape. a)Shifting of the TES training region composition from basalt to dust and b) the resulting chloride unit spectral shape. c) Shifting of the TES training region composition from Surface Type 1 (ST1) to Surface Type 2 (ST2) and the resulting chloride unit spectral shape.

to dust and from Surface Type 1 (terrestrial basalt) to Surface Type 2 (basaltic andesite to andesite) [*Bandfield et al.*, 2000]. The spectra of these modeled TES training region surface compositions and the resulting chloride unit spectral shapes can be observed in Figure 3-13. A purely basaltic TES training region will result in chloride unit spectral shape with an emissivity minimum at band 5 while a completely dusty surface selected as the TES training region will result in a chloride unit spectra with an emissivity maximum located at band 5. As the TES training region surface composition is shifted from ST1 to ST2, the resulting chloride unit spectral shape shifts from having a broad emissivity minimum centered at band 7 to a narrow emissivity minimum centered at band 5. These changes in the TES training region surface composition should not result in changes in the resulting surface emissivity values if the atmospheric correction is effectively removing the atmospheric component.

3.5 Conclusions

This study characterized the effects of the choice of a TES training region used in the atmospheric correction and the THEMIS observation conditions on the spectral character of chloride units. This study has demonstrated that more work needs to be conducted to examine other possible effects that are occurring in the process of collecting, correcting and analyzing THEMIS images. In order to ensure that the spectra observed are indicating surface mineralogy, the effects of data collection and processing need to be removed.

Overall, spectral variability plots indicated that the spectral and temperature properties of the TES training region do not have a strong relationship with the resulting THEMIS chloride unit spectral slopes. However, large variations in chloride unit spectral slopes can occur due to the choice of the TES training region. The slight correlation observed in the plot of average chloride unit slope versus TES training region minimum emissivity may be clarified upon further

investigation. Examination of individual THEMIS images using different TES training regions further supported this lack of a close association between TES training region choice and spectral character. The use of overlapping THEMIS images with the same TES region used for the atmospheric correction revealed that variation does not originate solely from THEMIS data collection conditions either. All of these observations indicate that there must be another element that has an influence on the spectral character which must be discovered and accounted for before the emissivity of these deposits can be fully representative of the surface mineralogy alone.

Spectral models of the effect of TES training region composition and derived atmospheric component spectra reveal that the current manual atmospheric correction technique using TES regions overlapping the THEMIS image is insufficient. This is likely due to the chosen TES training region emissivity values being incorrect due to an incomplete spectral library used in the process of deconvolving the surface compositions.

Future work to understand all of the elements affecting the spectral character of THEMIS emissivity images is imperative. Comparison with TES data from the larger chloride units could illuminate the differences between the multispectral corrected THEMIS emissivity data and the hyperspectral TES data.

4. Conclusions and Future Work

The work presented in this thesis was performed with the goal of increasing our understanding of the spectral character of chloride deposits observed by both Mars Odyssey's THEMIS and MRO's CRISM instruments. By addressing the variation in mid IR chloride unit spectral character that is not a due to surface mineralogy in THEMIS data and emulating the NIR spectral character of chloride deposits in the laboratory using mineral/rock mixtures, some of the confusion surrounding these deposits has been clarified.

In Chapter 2, the NIR laboratory study conducted to emulate the spectral character of chloride-bearing units observed by CRISM revealed some constraints on the composition and grain size. This study ruled out the possibility of unoxidized sulfide being a component in these deposits and supported the presence of an anhydrous chloride mineral. The halite mixtures with labradorite were successful in producing red sloping featureless ratio spectra for all proportions and grain sizes except for the ≤10 μm grain size mixtures with halite proportions of 1-5 wt.%. The halite crusts on labradorite were successful for all grain sizes studied except for the 63-90 μm. The use of labradorite served as a simple case involving only one mineral being mixed with halite and it is not likely that chlorides on the surface of Mars would be mixed with only labradorite. The halite mixtures with flood basalt are more realistic for the surface of Mars and the conditions under which these mixtures successfully emulated the CRISM ratio spectra were more limited. Only halite mixtures with flood basalt of 1-25 wt. % halite and grain sizes of 63-90 and 125-180 μm were able to imitate the desired spectral shape. Halite crusts on flood basalt were successful for the 125-180 and 250-355 μm grain sizes. Whereas there were absorptions present in the ratio spectra for most of the successful compositions analyzed, they can all be explained by the presence of small amounts of water or a muscovite impurity in the case of

labradorite-bearing samples. The flood basalt results correlate nicely with thermal inertia calculations for these deposits that indicate that these chloride deposits are either composed of materials of large grain size (~900 μm) or are indurated [*Presley and Christensen,* 1997; *Mellon et al*., 2000; *Putzig et al*., 2005; *Osterloo et al*., 2010]. These results are a promising beginning in constraining the possible chloride abundance and composition of these Martian deposits.

The study conducted in Chapter 3 revealed that the spectral variation resulting from TES training regions manually selected to correct for atmospheric attenuation in the THEMIS data and resulting from different data collection conditions observed through overlapping THEMIS images cannot currently be accounted for and separated from the data. The only property of the TES training region that has any correlation with the chloride unit spectral slope is the minimum emissivity derived from the corrected THEMIS data of the TES training region, and this is a very weak correlation. All locality and surface temperature variations of the TES training region did not result in predictable variations in the chloride unit spectral slope. The variability in the chloride unit spectral slope observed using multiple THEMIS images overlapping a chloride unit was also unpredictable and independent of seasonal and surface temperature variations between images. Simple models altering the TES training region composition and the magnitude of the atmospheric component removed in the manual atmospheric correction results in alteration of the chloride unit spectral shape and reveal that the atmospheric correction is not effective. Further investigation into other conditions that may cause changes in spectral character needs to be conducted so that the mineralogy of these deposits is the only component causing spectral changes between deposits.

Many studies could be conducted to further our understanding of Martian chloride deposits. A laboratory study in longer wavelength regions is currently being conducted using

mixtures similar to those used in Chapter 2 in an effort to place further constraints on the grain size and chloride abundance that is present in these deposits. If variation occurs from the use of other anhydrous chloride minerals in the mixtures, it could allow a spectral library to be assembled to compare with the remote sensing spectral character. The use of available TES data from the largest chloride units could help to reveal a more detailed view of the chloride unit spectral slopes observed by THEMIS.

References

Bandfield, J. L. (2009), Effects of surface roughness and graybody emissivity on martian thermal infrared spectra, *Icarus*, *202*(2), 414-428, doi:10.1016/j.icarus.2009.03.031.

Bandfield, J. L., V. E. Hamilton, and P. R. Christensen (2000), A Global View of Martian Surface Compositions from MGS-TES, *Science*, *287*(5458), 1626-1630, doi:10.1126/science.287.5458.1626.

Bandfield, J. L., D. Rogers, M. D. Smith, and P. R. Christensen (2004), Atmospheric correction and surface spectral unit mapping using Thermal Emission Imaging System data, *Journal of Geophysical Research*, *109*, E10008, doi:10.1029/2004je002289.

Bernard, A., and F. Le Guern (1986), Condensation of volatile elements in high-temperature gases of Mount St. Helens, *J. Volcan. Geotherm. Res.*, *28*(1-2), 91-105, doi:10.1016/0377-0273(86)90007-7.

Bridges, J. C., and M. M. Grady (1999), A halite-siderite-anhydrite-chlorapatite assemblage in Nakhla: Mineralogical evidence for evaporites on Mars, *Meteorit. Planet. Sci.*, *34*(3), 407-415, doi:10.1111/j.1945-5100.1999.tb01349.x.

Bridges, J. C., and M. M. Grady (2000), Evaporite mineral assemblages in the nakhlite (martian) meteorites, *Earth Planet. Sci. Lett.*, *176*(3-4), 267-279, doi:10.1016/S0012-821X(00)00019-4.

Bridges, J. C., D. C. Catling, J. M. Saxton, T. D. Swindle, I. C. Lyon, and M. M. Grady (2001), Alteration assemblages in martian meteorites: Implications for near-surface processes, *Space Sci. Rev.*, *96*(1-4), 365-392, doi:10.1023/A:1011965826553.

Brückner, J., G. Dreibus, R. Rieder, and H. Wänke (2003), Refined data of Alpha Proton X-ray Spectrometer analyses of soils and rocks at the Mars Pathfinder site: Implications for surface chemistry, *J. Geophys. Res.*, *108*(E12), 8094, doi:10.1029/2003je002060.

Burgess, R., I. P. Wright, and C. T. Pillinger (1989), Distribution of sulphides and oxidised sulphur components in SNC meteorites, *Earth Planet. Sc. Lett.*, *93*(3-4), 314-320, doi:10.1016/0012-821x(89)90030-7.

Burns, R. G., and D. S. Fisher (1990), Evolution of Sulfide Mineralization on Mars, *J. Geophys. Res.*, *95*(B9), 14169-14173, doi:10.1029/JB095iB09p14169.

Burns, R. G., and D. S. Fisher (1993), Rates of Oxidative Weathering on the Surface of Mars, *J. Geophys. Res.*, *98*(E2), 3365-3372, doi:10.1029/92JE02055.

Chevrier, V., P. Rochette, P. E. Mathe, and O. Grauby (2004), Weathering of iron-rich phases in simulated Martian atmospheres, *Geology*, *32*(12), 1033-1036, doi:10.1130/G21078.1.

Christensen, P. R., J. L. Bandfield, V. E. Hamilton, D. A. Howard, M. D. Lane, J. L. Piatek, S. W. Ruff, and W. L. Stefanov (2000), A thermal emission spectral library of rock-forming minerals, *J. Geophys. Res., 105*(E4), 9735-9739, doi:10.1029/1998je000624.

Clark, B. C., A. K. Baird, R. J. Weldon, D. M. Tsusaki, L. Schnabel, and M. P. Candelaria (1982), Chemical-Composition of Martian Fines, *J. Geophys. Res., 87*(NB12), 59-67, doi:10.1029/JB087iB12p10059.

Clark, R. N., G. A. Swayze, R. Wise, E. Livo, T. Hoefen, R. Kokaly, and S. J. Sutley (2007), USGS digital library splib06a: U.S. Geological Survey, *Digital Data Series 231*, (Available at http://speclab.cr.usgs.gov/spectral.lib06).

Day, P. R. (1965), Particle fractionation and particle -size analysis, in *Methods of Soil analysis, Part 1: Physical and Mineralogical Properties, Including Statistics of Measurement and Sampling*, edited by C. A. Black, D. D. Evans, L. E. Ensminger, J. L. White and F. E. Clark, pp. 545-567, American Society of Agronomy, Inc., Madison.

Deer, W. A., R. A. Howie, and J. Zussman (1992), *An Introduction to Rock-Forming Minerals*, 2nd ed., 696 pp., Pearson Education Limited, Harlow.

Elsetinow, A. R., M. J. Borda, M. A. A. Schoonen, and D. R. Strongin (2003), Suppression of pyrite oxidation in acidic aqueous environments using lipids having two hydrophobic tails, *Advances Environ. Res., 7*(4), 969-974, doi:10.1016/s1093-0191(02)00101-6.

Eugster, H. P., and L. A. Hardie (1978), Saline Lakes, in *Lakes: Chemistry, Geology, Physics*, edited by A. Lerman, pp. 237-293, Springer-Verlag, New York.

Fleischer, I., et al. (2010), Mineralogy and chemistry of cobbles at Meridiani Planum, Mars, investigated by the Mars Exploration Rover Opportunity, *J. Geophys. Res., 115*, E00F05, doi:10.1029/2010je003621.

Gee, G. W., and J. W. Bauder (1986), Particle-Size Analysis, in *Methods of Soil Analysis, Part 1: Physical and Mineralogical Methods*, edited by A. Klute, American Society of Agronomy, Inc. Soil Science Society of America, Inc., Madison.

Gellert, R., et al. (2006), Alpha particle X-ray spectrometer (APXS): Results from Gusev crater and calibration report, *J. Geophys. Res., 111*(E2), E02S05, doi:10.1029/2005je002555.

Gillespie, A. R., A. B. Kahle, and R. E. Walker (1986), Color Enhancement of Highly Correlated Images .1. Decorrelation and Hsi Contrast Stretches, *Remote Sens. Environ., 20*(3), 209-235, doi:10.10160034-4257(86)90044-1.

Glotch, T. D., J. L. Bandfield, L. L. Tornabene, H. B. Jensen, and F. P. Seelos (2010), Distribution and formation of chlorides and phyllosilicates in Terra Sirenum, Mars, *Geophys. Res. Lett., 37*, L16202, doi:10.1029/2010gl044557.

Goodall, T. M., C. P. North, and K. W. Glennie (2000), Surface and subsurface sedimentary structures produced by salt crusts, *Sedimentology*, *47*(1), 99-118, doi:10.1046/j.1365-3091.2000.00279.x.

Gooding, J. L., K. E. Aggrey, and D. W. Muenow (1990), Volatile compounds in shergottite and nakhlite meteorites, *Meteoritics*, *25*, 281-289.

Gooding, J. L., S. J. Wentworth, and M. E. Zolensky (1991), Aqueous Alteration of the Nakhla Meteorite, *Meteoritics*, *26*(2), 135-143.

Guilbert, J. M., and C. F. J. Park (1986), *The Geology of Ore Deposits*, 985 pp., W. H. Freeman and Company, New York.

Hardie, L. A., J. P. Smoot, and H. P. Eugster (1978), Saline Lakes and their Deposits: A Sedimentological Approach, in *Modern and Ancient Lake Sediments*, edited by A. Matter and M. E. Tucker, pp. 7-41, Blackwell Scientific Publications, Oxford, UK.

Hecht, M. H., et al. (2009), Detection of Perchlorate and the Soluble Chemistry of Martian Soil at the Phoenix Lander Site, *Science*, *325*(5936), 64-67, doi: 10.1029/2006je002881.

Hem, J. D. (1992), Study and interpretation of the chemical characteristics of natural water, edited, p. 363, U.S. Govt. Print. Off..

Hunt, G. R., J. W. Salisbury, and C. J. Lenhoff (1971), Visible and near-infrared spectra of minerals and rocks, IV. Sulphides and sulphates, *Modern Geology*, *2*, 23-30.

Hunt, G. R., J. W. Salisbury, and C. J. Lenhoff (1972), Visible and near-infrared spectra of minerals and rocks, V. Halides, arsenates, vanadates, and borates, *Modern Geology*, *3*, 121-132.

Jambor, J. L., D. K. Nordstrom, and C. N. Alpers (2000), Metal-sulfate Salts from Sulfide Mineral Oxidation, in *Sulfate Minerals: Crystallography, Geochemistry, and Environmental Significance*, edited by C. N. Alpers, J. L. Jambor and D. K. Nordstrom, pp. 303-350, Mineralogical Society of America, Washington, DC.

Jensen, H. B., and T. D. Glotch (2011), Investigation of the near infrared spectral character of putative Martian chloride deposits, *J. Geophys. Res.*, *in review*.

Karthe, S., R. Szargan, and E. Suoninen (1993), Oxidation of pyrite surfaces: a photoelectron spectroscopic study, *Applied Surface Science*, *72*(2), 157-170, doi:10.1016/0169-4332(93)90007-x.

Kounaves, S. P., et al. (2010), Soluble sulfate in the martian soil at the Phoenix landing site, *Geophys. Res. Lett.*, *37*(9), L09201, doi: 10.1029/2010gl042613.

Lorand, J. P., V. Chevrier, and V. Sautter (2005), Sulfide mineralogy and redox conditions in some shergottites, *Met. Planet. Sci.*, *40*(8), 1257-1272, doi:10.1111/j.1945-5100.2005.tb00187.x.

McGuire, P. C., et al. (2009), An improvement to the volcano-scan algorithm for atmospheric correction of CRISM and OMEGA spectral data, *Planet. Space Sci.*, *57*(7), 809-815, doi:10.1016/j.pss.2009.03.007.

McSween, H. Y., Jr. (1985), SNC meteorites: Clues to Martian petrologic evolution?, *Rev. Geophys.*, *23*(4), 391-416, doi:10.1029/RG023i004p00391.

Mellon, M. T., B. M. Jakosky, H. H. Kieffer, and P. R. Christensen (2000), High-Resolution Thermal Inertia Mapping from the Mars Global Surveyor Thermal Emission Spectrometer, *Icarus*, 148(2), 437-455, doi:10.1006/icar.2000.6503.

Milliken, R. E., and D. L. Bish (2010), Sources and sinks of clay minerals on Mars, *Philos. Mag.*, *90*(17-18), 2293-2308, doi:10.1080/14786430903575132.

Ming, D. W., et al. (2008), Geochemical properties of rocks and soils in Gusev Crater, Mars: Results of the Alpha Particle X-Ray Spectrometer from Cumberland Ridge to Home Plate, *J. Geophys. Res.*, *113*(E12), E12S39, doi:10.1029/2008je003195.

Murchie, S. L., et al. (2009), A synthesis of Martian aqueous mineralogy after 1 Mars year of observations from the Mars Reconnaissance Orbiter, *J. Geophys. Res*, *114*, E00D06, doi:10.1029/2009je003342.

Osterloo, M. M., F. S. Anderson, V. E. Hamilton, and B. M. Hynek (2010), Geologic context of proposed chloride-bearing materials on Mars, *J. Geophys. Res.-Planets*, *115*, E10012, doi:10.1029/2010je003613.

Osterloo, M. M., V. E. Hamilton, J. L. Bandfield, T. D. Glotch, A. M. Baldridge, P. R. Christensen, L. L. Tornabene, and F. S. Anderson (2008), Chloride-bearing materials in the southern highlands of Mars, *Science*, *319*(5870), 1651-1654, doi:10.1126/science.1150690.

Pelkey, S. M., et al. (2007), CRISM multispectral summary products: Parameterizing mineral diversity on Mars from reflectance, *J. Geophys. Res.*, *112*(E8), E08S14, doi:10.1029/2006je002831.

Presley, M. A., and P. R. Christensen (1997), Thermal conductivity measurements of particulate materials 2. Results, *J. Geophys. Res.*, 102(E3), 6551-6566, doi:10.1029/96je03303.

Putzig, N. E., M. T. Mellon, K. A. Kretke, and R. E. Arvidson (2005), Global thermal inertia and surface properties of Mars from the MGS mapping mission, *Icarus*, 173(2), 325-341, doi:10.1016/j.icarus.2004.08.017.

Rieder, R., et al. (2004), Chemistry of Rocks and Soils at Meridiani Planum from the Alpha Particle X-ray Spectrometer, *Science*, *306*(5702), 1746-1749, doi:10.1126/science.1104358.

Rogers, A. D., and P. R. Christensen (2007), Surface mineralogy of Martian low-albedo regions from MGS-TES data: Implications for upper crustal evolution and surface alteration, J. *Geophys. Res.*, *112*(E1), E01003, doi:10.1029/2006je002727.

Salemi, E., U. Tessari, N. Colombani, and M. Mastrocicco (2010), Improved gravitational grain size separation method, *App.l Clay. Sci.*, *48*(4), 612-614,doi:10.1016/j.clay.2010.03.014.

Schröder, C., et al. (2008), Meteorites on Mars observed with the Mars Exploration Rovers, *J. Geophys. Res.*, *113*(E6), E06S22, doi:10.1029/2007je002990.

Schröder, C., et al. (2010), Properties and distribution of paired candidate stony meteorites at Meridiani Planum, Mars, *J. Geophys. Res.*, *115*, E00F09, doi:10.1029/2010je003616.

Squyres, S. W., et al. (2007), Pyroclastic Activity at Home Plate in Gusev Crater, Mars, *Science*, *316*(5825), 738-742, doi:10.1126/science.1139045.

Swayze, G. A., et al. (2000), Using Imaging Spectroscopy To Map Acidic Mine Waste, *Environ. Sci. Tech.*, *34*(1), 47-54, doi:10.102/es990046w.

Symonds, R. B., W. I. Rose, M. H. Reed, F. E. Lichte, and D. L. Finnegan (1987), Volatilization, transport and sublimation of metallic and non-metallic elements in high temperature gases at Merapi Volcano, Indonesia, *Geochim. Cosmochim. Acta*, *51*(8), 2083-2101, doi:10.106/0016-7037(87)90258-4.

Tanaka, K. L. (1986), The Stratigraphy of Mars, *J. Geophys. Res.*, *91*(B13), E139-E158, doi:10.1029/JB091iB13p0E139.

Tanaka, K. L., and W. K. Hartmann (2008), The planetary timescale, in *The Concise Geologic Time Scale*, edited by J. G. Ogg, G. M. Ogg and F.M. Gradstein, pp. 13-22, Cambridge University Press, New York.

Weiss-Malik, M., N. S. Gorelick, and P. R. Christensen (2005), JMARS: A GIS System for Mars and Other Planets, *Eos Trans. AGU (Fall Meet. Suppl.)*, *86*, P21C-0169.

Wray, J. J., S. L. Murchie, S. W. Squyres, F. P. Seelos, and L. L. Tornabene (2009), Diverse aqueous environments on ancient Mars revealed in the southern highlands, *Geology*, *37*(11), 1043-1046, doi:10.1130/G30331a.1.

Zolotov, M. Y., and E. L. Shock (2005), Formation of jarosite-bearing deposits through aqueous oxidation of pyrite at Meridiani Planum, Mars, *Geophys. Res. Lett.*, *32*(21), L21203, doi:10.1029/2005GL024253.